The Astrophysical Journal, 962:18 (26pp), 2024 February 10 https://doi.org/10.3847/1538-4357/ad0ecc

Jump-starting Relativistic Flows and the M87 Jet

Maxim Lyutikov and Ahmad Ibrahim
Department of Physics and Astronomy, Purdue University, 525 Northwestern Avenue, West Lafayette, IN 47907-2036, USA
Received 2023 May 25; revised 2023 November 12; accepted 2023 November 20; published 2024 February 1

Abstract

We point out the dominant importance of plasma injection effects of relativistic winds from pulsars and black holes. We demonstrate that outside the light cylinder, the magnetically dominated outflows sliding along the helical magnetic field move nearly radially with very large Lorentz factors, $\gamma_0 \gg 1$, imprinted into the flow during pair production within the gaps. Only at larger distances, $r \geqslant \gamma_0(c/\Omega)$, does MHD acceleration $\Gamma \propto r$ take over. As a result, Blandford–Znajek (BZ)-driven outflows produce spine-brightened images. The best-resolved case of the jet in M87 shows both edge-brightened features, as well as weaker spine-brightened features. Only the spine-brightened component can be BZ driven/originate from the black hole's magnetosphere.

Unified Astronomy Thesaurus concepts: Relativistic jets (1390)

1. Introduction

Acceleration of relativistic winds and jets is a classical problem in high-energy astrophysics (e.g., Michel 1969; Goldreich & Julian 1970; Blandford & Znajek 1977; Blandford & Königl 1979; Camenzind 1986; Krolik 1999; McKinney 2006; Barkov & Komissarov 2008; Blandford et al. 2019). A standard approach involves the solution of the MHD equation (analytical or numerical) starting with a slowly moving plasma. Plasma is then accelerated by the corresponding pressure gradient, and collimated by magnetic hoop stresses (Blandford & Payne 1982).

Observations of the inner part of the jet in M87, down to just 7 Schwarzschild radii, show a complicated structure. First, one observes a limb-brightened collimated jet—the jet accelerating smoothly, with a parabolic profile (Nakamura & Asada 2013; Kim et al. 2018; Blandford et al. 2019; Figure 1).

In addition to limb-brightened structures, Lu et al. (2023) recently detected a new feature—a spine-brightened jet.

In this work, we aim to model the emission pattern expected in the Blandford–Znajek (BZ; Blandford & Znajek 1977) model of jet acceleration and compare it with the observation. The key new ingredient in our work is taking into account large initial (injection) velocities parallel to the local magnetic field.

MHD models of acceleration (Beskin 2009; Komissarov et al. 2009; Nokhrina & Beskin 2017) take into full account the plasma velocity: both along and across the magnetic field. The corresponding analytical treatment, based on the relativistic Grad–Shafranov equation (Shafranov 1966; Grad 1967; Scharlemann & Wagoner 1973; Beskin 2009) is completed, as it requires finding the initially unknown current distribution together with the solution for the magnetic field.

In the limit of highly magnetized plasma—the force-free limit—the parallel velocity is not defined in principle. But that does not mean it can be neglected. Plasma may be/is streaming with large Lorentz factors along magnetic fields. It seems this particular aspect has not been considered previously. But it is highly important as we argue here.

Models of gaps in black hole magnetospheres (Blandford & Znajek 1977; Hirotani & Okamoto 1998; Levinson 2000; Levinson & Rieger 2011; Ptitsyna & Neronov 2016) generally predict that magnetospheric gaps, with thicknesses much smaller than the size of the magnetosphere (the light cylinder) accelerate particles with Lorentz factors of $\sim 10^3$–10^4; accelerated particles first inverse Compton (IC) scatter soft disk photons, and is followed by two-photon pair production and the electromagnetic cascade. The resulting Lorentz factors are of similar values, $\sim 10^3$–10^4. Lorentz factors up to $\sim 10^6$ are also possible (Ptitsyna & Neronov 2016).

In MHD simulations, first, high magnetization is hard to achieve and, second, plasma is typically injected at rest (e.g., Tomimatsu 1994). In the corresponding particle-in-cell (PIC) simulations particles are typically injected at rest (e.g., Chen & Beloborodov 2014; Philippov et al. 2015; Crinquand et al. 2020; Hakobyan et al. 2023).

Perhaps the closest approach to the current one is that in Beskin & Kuznetsova (2000), where the importance of injection for the structure of the magnetosphere and the corresponding energy relations were discussed. "It is the pair creation region that plays the role of the energy 'source'" (Beskin et al. 1992, is also relevant).

2. Approach and Conclusion

We start with a force-free solution and add particle dynamics along the field kinematically, in the bead-on-wire approximation, neglecting its back reaction on the structure of the magnetic field. The bead-on-wire approach has a clear advantage: for a given structure of the magnetic field the particle dynamics is easily calculated in algebraic form (see also Section 7.2.6 of Gralla & Jacobson 2014). No integration of the equations of motion is needed and no special conditions (e.g., at Alfvén or fast surfaces) appear. The drawback is that it does not provide the full picture of what the magnetic field structure is: the structure of the magnetosphere should be prescribed. Thus, our approach can be seen as the next term in the expansion in the magnetization

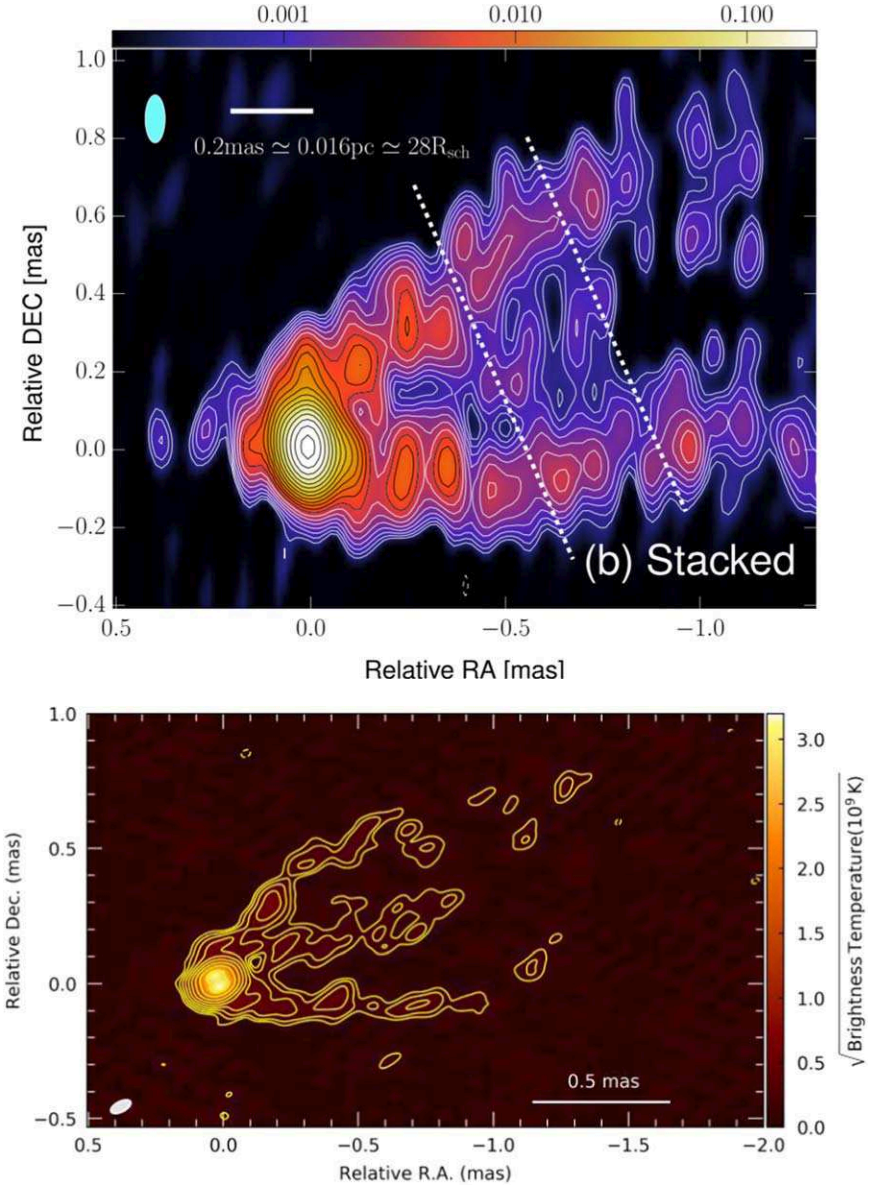

Figure 1. Top: central part of the jet in M87 at 86 GHz showing a limb-brightened jet (Kim et al. 2018). Bottom: spine-brightened structure (Lu et al. 2023).

parameter $1/\sigma \ll 1$: a force-free solution in the limit of $1/\sigma \to 0$ provides the structure of the magnetic field, and the next term takes into account particle dynamics in the prescribed magnetic field.

To start, we assume that flow lines and magnetic flux surfaces are conical. (More complicated collimated flux surfaces behave similarly, see Section 5.1.) In flat metrics, there is then an analytical solution for the monopolar magnetic field due to Michel's (1973) solution (it can be generalized to the Schwarzschild case). We use it as a starting point:

$$
\begin{aligned}
B_r &= \frac{r_0^2}{r^2} B_0 \\
B_\phi &= -\frac{r_0^2 \sin\theta\Omega}{r} B_0 = E_\theta \\
\beta_{\rm EM} &= \left\{ \frac{r^2 \sin^2\theta\Omega^2}{1 + r^2 \sin^2\theta\Omega^2}, 0, \frac{r\Omega \sin(\theta)}{1 + r^2 \sin^2\theta\Omega^2} \right\} \\
\Gamma_{\rm EM} &= \sqrt{1 + r^2\Omega^2 \sin^2(\theta)}\,.
\end{aligned}
\tag{1}
$$

This analytical force-free solution of the pulsar equation (Scharlemann & Wagoner 1973; Beskin 2009) passes smoothly through the light cylinder (Alfvén surface) $R_{\rm LC} = c/(\sin\theta\Omega)$. Numerical models of the inner wind indicate that the structure of the electromagnetic fields quickly approaches Michel's solution (Prokofev et al. 2018). Komissarov (2004) showed that the monopolar geometry of magnetic field lines is also a good approximation in the case of a black hole in an external magnetic field.

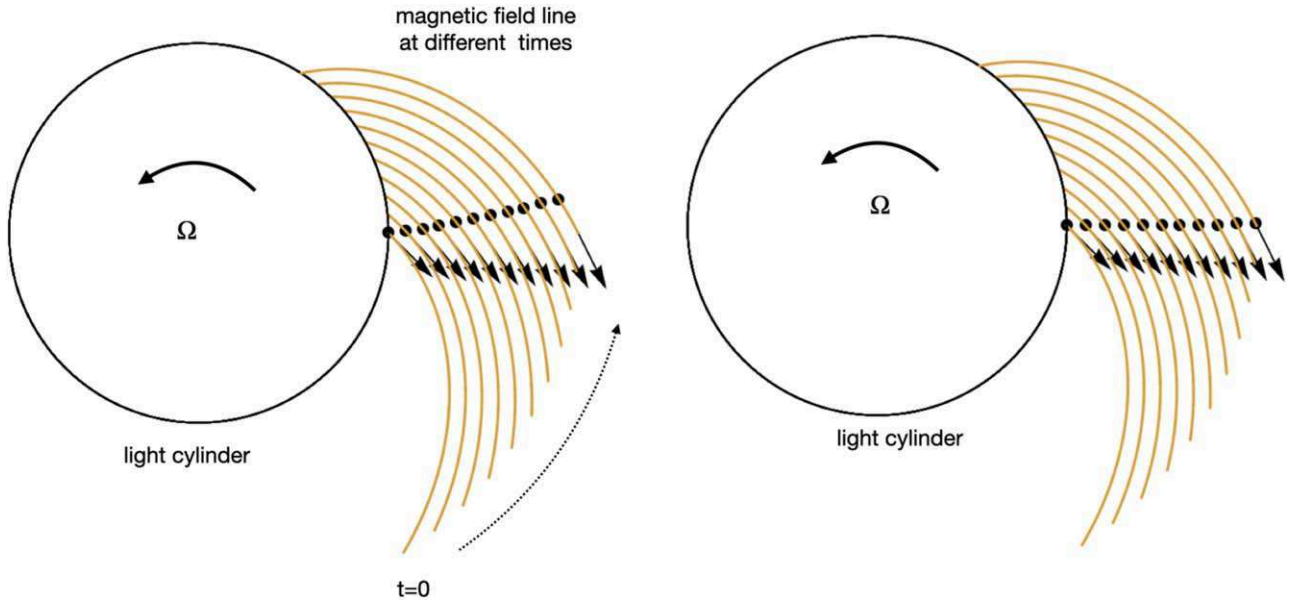

Figure 2. Particle trajectories calculated in Michel's field outside the light cylinder for Lorentz factors $\gamma_0 = 2$, 10, Equation (A7). The circle represents the light cylinder, the orange curves indicate the same magnetic field line at consecutive movements, the arrows indicate the directions of the particle velocity at each point, and the black dots denote the location of the particle. These calculations illustrate that for $\gamma_0 \gg 1$ the trajectory is nearly radial.

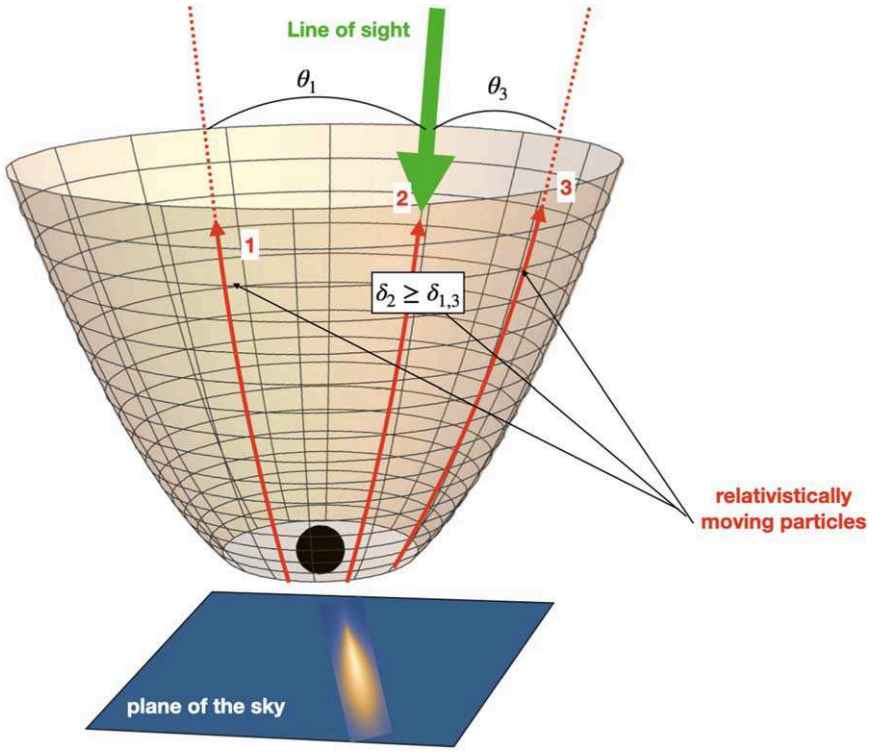

Figure 3. Graphic explanation of why BZ-produced jets are expected to be spine brightened. Shown are flux surfaces and three different particle trajectories. The emission produced by particle 2 has the smallest angle with respect to the line of sight, the largest Doppler factor, and result in the brightest emission pattern.

As long as the force-free condition is satisfied (negligible inertial effects) arbitrary initial motion of (charge-neutral) plasma can be added along the field. Conditions at the light cylinder remain unchanged. The total velocity is then the (relativistic) sum of the electromagnetic velocity (Equation (1)) and the motion along the rotating magnetic field.

It turns out that a particle launched with a large Lorentz factor along the rotating magnetic spiral (in a bead-on-wire approximation) moves nearly radially (Figure 2). This is a known effect of numerical analysis (Contopoulos et al. 2020), and has recently been analytically discussed by Lyutikov (2022). The key point is that the azimuthal motion along the spiral is nearly compensated by the motion of the spiral itself. In this paper, we generalize the results of Lyutikov (2022) for particle dynamics in rotating winds to the curved space of Schwarzschild and Kerr black holes.

The observed emission pattern from relativistically moving particles is dominated by the Doppler factor δ. For an axisymmetric jet the largest Doppler factor is along the flow lines projected into the spine of the image, Figure 3.

Thus, relativistic flows emanating from within the magnetosphere, driven by the BZ process, are expected to produce a spine-brightened image. This is consistent with observations of a weak central spine in the M87 jet (Figure 1, bottom panel). On the other hand, the edge-brightened emission observed by Kim et al. (2018) is inconsistent with the BZ process. The edge-brightened part is not centered on the black hole. This implies that a flow is only mildly relativistic. For example, estimates of the viewing angle of 15°–30° (Bicknell & Begelman 1996) imply bulk Lorentz factors of ∼3–2 (otherwise the emission would have been beamed away).

We then conclude that the limb-brightened and spine-brightened parts of the M87 jet have different origins: the spine-brightened part originates within the black hole magnetosphere driven by the BZ mechanism. The edge-brightened component should have a different origin. For example, it can be produced by the Blandford & Payne (1982) mechanism, starting as a slow accelerating flow from the accretion disk.

3. Particle Motion along a Rotating Spiral

3.1. General Relations

The motion of a particle in bead-on-wire approximation can be derived algebraically for a given structure of magnetosphere in the case of flat, Schwarzschild, and Kerr metrics. As a basic case, we start with particles moving in the equatorial plane in the case of the Kerr metric. We start with a particular case of an Archimedean spiral with a radial step equal to $1/\Omega$.

We use the machinery of general relativity to treat particle motion in the rotating frame, in curved spacetime. We start at the equatorial plane of $\theta = \pi/2$ of the Kerr metric. For the flat and Schwarzschild cases, where a monopolar magnetic field is an exact solution, the generalization to motion with a fixed arbitrary polar angle is recovered later.

The results of this section are further re-derived/extended in the appendices. In Appendix A we re-derive the corresponding relations using Lagrangian and Hamiltonian approaches for relativistic particles moving along a constrained path in flat spacetime. In Appendix B, we use an alternative formulation of the Lagrangian. In Section 3.5, we allow for arbitrary radial steps (effective, taking into account non-force-free effects of plasma loading). Finally, in the most mathematically advanced approach, in Appendix D we discuss the most general case of field structure in the Kerr metric.

The Kerr metric in the equatorial plane is defined by the metric tensor

$$\begin{aligned} g_{00} &= 1 - \frac{2M}{r} = \alpha^2 \\ g_{rr} &= \frac{r^2}{\Delta} \\ g_{\phi\phi} &= a^2M^2 + r^2 + \frac{2a^2M^3}{r} \equiv \Delta_1 \\ g_{0\phi} &= -\frac{2aM^2}{r} \\ \Delta &= a^2M^2 - 2Mr + r^2 \\ \Delta_1 &= a^2M^2 + r^2 + \frac{2a^2M^3}{r}, \end{aligned} \tag{2}$$

where a is the dimensionless Kerr parameter.

Consider rotating the black hole magnetosphere. Since we use a bead-on-wire approximation, we first need to find the structure of a given magnetic field line. The rotating spiral is defined by two parameters: the angular velocity of rotation Ω and radial step c/Ω_1. In the force-free approximation, $\Omega = \Omega_1$ (see Section 3.5 for a generalization $\Omega_1 \neq \Omega$), the fast electromagnetic mode propagates radially with (setting $ds = 0$ for the null trajectory and $d\phi = 0$ for the radial propagation)

$$\beta_F = \sqrt{\frac{\Delta(r-2M)}{r^3}} = \frac{\alpha\sqrt{\Delta}}{r} \to \alpha^2 \tag{3}$$

(the latter limit is for the Schwarzschild case).

The angular velocity of the Lense–Thirring precession is

$$\omega_{LT} = a\frac{2M^2}{r^3 + a^2M^2(2M+r)} = \frac{2aM^2}{r\Delta_1} = -\frac{g_{0\phi}}{g_{\phi\phi}}. \tag{4}$$

Thus, the radial step of the spiral is given by

$$\begin{aligned} d\phi' &= \omega_{\rm sp} dr \\ \omega_{\rm sp} &= \frac{\omega_{LT} - \Omega}{\beta_F} = -\sqrt{\frac{g_{rr}}{g_{00}}}\left(\frac{g_{0\phi}}{g_{\phi\phi}} + \Omega\right). \end{aligned} \tag{5}$$

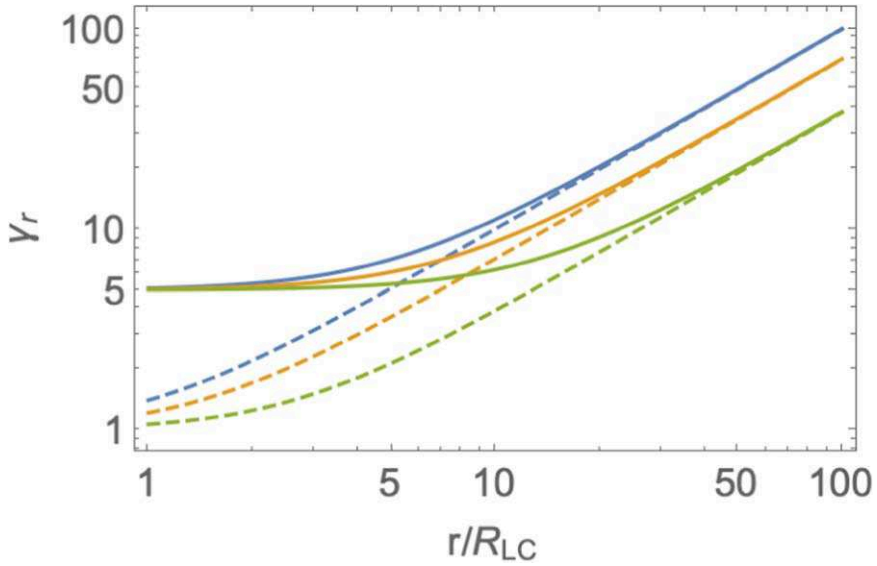

Figure 4. Lorentz factors corresponding to Equation (18) compared with Michel's solution $\gamma = \sqrt{1 + r^2\Omega^2 \sin^2\theta}$ for $\gamma_0 = 5$ and $\theta = \pi/8, \pi/4, \pi/2$ (bottom to top). Only at large distances does $r \geqslant \gamma_0 R_{LC}$ MHD acceleration pick up.

(For propagation with subluminal velocity, see Section 3.5. In this case, the radial step is smaller than $1/\Omega$. This can be due to the back reaction of plasma on magnetic field lines.)

Next, in the Kerr metric, transferring to the frame rotating with the magnetic field (see Appendix C for corresponding limitations)

$$d\phi \to d\phi' + \Omega dt \tag{6}$$

and imposing the spiral constraint (Equation (5)), we find the metric coefficients in the rotating frame of

$$\begin{aligned} G_{00} &= g_{00} - \left(g_{\phi\phi}\Omega - \frac{4aM^2}{r}\right)\Omega \\ G_{rr} &= \frac{r^2}{\Delta} + g_{\phi\phi}\omega_{\rm sp}^2 \\ G_{0r} &= \left(-\frac{2aM^2}{r} + \Omega\, g_{\phi\phi}\right)\omega_{\rm sp}. \end{aligned} \tag{7}$$

The contra-variant metric is

$$\begin{aligned} G^{00} &= -\frac{G_{rr}}{\Delta_G} \\ G^{rr} &= \frac{G_{00}}{\Delta_G} \\ G^{0r} &= \frac{G_{0r}}{\Delta_G} \\ \Delta_G &= G_{0r}^2 + G_{00}G_{rr}. \end{aligned} \tag{8}$$

Using the Hamilton–Jacobi equation

$$G^{00}(\partial_t S)^2 + 2G^{0r}(\partial_t S)(\partial_r S) + G^{rr}(\partial_r S)^2 = 1 \tag{9}$$

with a separation of

$$S = -\gamma_0 t + S_1(r), \tag{10}$$

we find

$$G^{00}\gamma_0^2 - 2G^{0r}\gamma_0(\partial_r S) + G^{rr}(\partial_r S)^2 = 1. \tag{11}$$

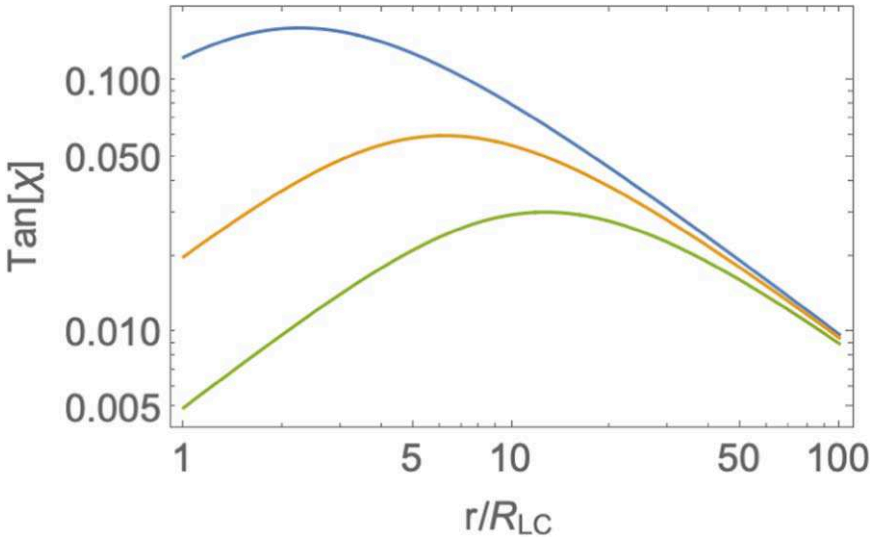

Figure 5. Angle of motion with respect to the radial direction, $\tan\chi = \beta_\phi/\beta_r$ for $\gamma_0 = 2, 5, 10$ (top to bottom); flat space $M = 0$. The motion is nearly radial.

Thus,

$$(\partial_r S) = \frac{G_{0r}}{G_{00}}\gamma_0 \pm \frac{\sqrt{\Delta_G(\gamma_0^2 - G_{00})}}{G_{00}}. \tag{12}$$

This equation can be analytically integrated into flat space, giving the trajectory $r(t)$ (Lyutikov 2022); see also an alternative derivation in Appendix A, Equation (A7). But deriving $r(t)$ is an unnecessary yet complicated step, since we are not interested in the time dependence of the particle velocity, only in its coordinate dependence.

Differentiating with respect to γ_0 gives

$$\partial_{\gamma_0}(\partial_r S) = \frac{G_{0r}}{G_{00}} \pm \frac{\gamma_0}{G_{00}}\sqrt{\frac{\Delta_G}{\gamma_0^2 - G_{00}}}. \tag{13}$$

Finally,

$$\beta_r = (\partial_{\gamma_0}(\partial_r S))^{-1} = \frac{G_{00}}{\gamma_0\sqrt{(G_{00}G_{rr} + G_{0r}^2)/(\gamma_0^2 - G_{00})} + G_{0r}}. \tag{14}$$

In Equation (14), we ignored the negative solution because it represents going in a noninteresting direction. We explain this more while re-deriving Equation (14) by various Lagrangian approaches in Appendices A and B. This solves the problem of particle dynamics in a rotating magnetosphere in the bead-on-wire approximation.

One of the mathematical complications involves changing the sign of G_{00} while crossing the light cylinder. However, the speed β_r stays positive. Explicit forms are given below, e.g., Equation (17), which passes smoothly through the light cylinder.

We point out that the Hamilton–Jacobi approach allows one to find the trajectory purely algebraically—no integration of the equation of motion is involved.

Next, we give explicit relations for particular examples of flat, Schwarzschild, and Kerr spaces.

3.2. *Flat Space* M = 0

In the frame rotating with the spiral the metric tensor is (see also Lyutikov 2022)

$$\begin{aligned} G_{00} &= 1 - \sin^2\theta r^2\Omega^2 \\ G_{0r} &= -\sin^2\theta r^2\Omega^2 \\ G_{rr} &= 1 + \sin^2\theta r^2\Omega^2 \end{aligned} \tag{15}$$

and gives the Christoffel coefficients

$$\begin{aligned}
\Gamma^0_{00} &= r^3 \sin^4\theta\Omega^4 \\
\Gamma^0_{0r} &= -r\sin^2\theta\Omega^2(1+\sin^2\theta r^2\Omega^2) \\
\Gamma^0_{rr} &= r\sin^2\theta\Omega^2(2+\sin^2\theta r^2\Omega^2) \\
\Gamma^r_{rr} &= r\sin^2\theta\Omega^2(1+\sin^2\theta r^2\Omega^2) \\
\Gamma^r_{0r} &= -r^3\sin^4\theta\Omega^4 \\
\Gamma^r_{00} &= -r\sin^2\theta\Omega^2(1-\sin^2\theta r^2\Omega^2)
\end{aligned} \tag{16}$$

$$\begin{aligned}
\beta_r &= \frac{1-\sin^2\theta r^2\Omega^2}{\frac{\gamma_0}{\sqrt{\gamma_0^2+\sin^2\theta r^2\Omega^2-1}}-\sin^2\theta r^2\Omega^2} \\
&= \begin{cases} 1-\dfrac{1}{2\gamma_0^2}, & \gamma_0 \gg r\Omega\sin\theta \\ 1-\dfrac{1}{\sin^2\theta r^2\Omega^2}+\dfrac{\gamma_0}{\sin^3\theta r^3\Omega^3}, & r\to\infty \\ \dfrac{2\gamma_0^2}{1+2\gamma_0^2}\approx 1-\dfrac{1}{2\gamma_0^2}, & r=1/\Omega \end{cases}.
\end{aligned} \tag{17}$$

The corresponding Lorentz factor $\gamma = 1\Big/\sqrt{1-\beta_r^2-(\sin\theta r\Omega(1-\beta_r))^2}$ is

$$\begin{aligned}
\gamma &= \frac{\gamma_0-\sin^2\theta r^2\Omega^2\sqrt{\gamma_0^2+\sin^2\theta r^2\Omega^2-1}}{1-\sin^2\theta r^2\Omega^2} \\
&= \begin{cases} \gamma_0+\dfrac{\sin^2\theta r^2\Omega^2}{2\gamma_0}, & \gamma_0 \gg r\Omega\sin\theta \\ \sin\theta r\Omega+\dfrac{1+\gamma_0^2}{2r\sin\theta\Omega}, & r\to\infty \\ \gamma_0+\dfrac{1}{2\gamma_0}+\dfrac{\sin\theta\Omega}{\gamma_0}\left(r-\dfrac{1}{\sin\theta\Omega}\right), & r\to 1/(\sin\theta\Omega) \end{cases}
\end{aligned} \tag{18}$$

(see Figure 4).

It may be verified using Lorentz transformations that the electric field in the frame of the particle is zero.

The integration constant γ_0 physically corresponds to some value of some energy at some location. With a change in parameter γ_0, so that $\gamma_0 + 1/(2\gamma_0) \to \gamma_{\rm LC}$, the solution would correspond to initial condition $\gamma_{\rm LC}$ on the light cylinder:

$$\beta_r = \frac{1-\sin^2\theta r^2\Omega^2}{\frac{\gamma_{\rm LC}+\sqrt{\gamma_{\rm LC}^2-2}}{2\sqrt{\frac{1}{4}(\gamma_{\rm LC}+\sqrt{\gamma_{\rm LC}^2-2})^2+\sin^2\theta r^2\Omega^2-1}}-\sin^2\theta r^2\Omega^2}. \tag{19}$$

In what follows we skip this unnecessary redefinition. Numerically γ_0 is typically very close to the energy of the particle crossing the outer light cylinder, see, e.g., Equation (17). Also, in Appendix (D) we discuss the range of the allowed values for this constant of motion and we show that this constant behaves the same as the initial Lorentz factor of a particle at the outer light cylinder when $\gamma_0 \gg 1$; hence, we give this constant the symbol γ_0.

Importantly, the toroidal component of the velocity always remains small,

$$\beta_\phi = \sin\theta r\Omega(1-\beta_r) = \frac{\gamma_0-\sqrt{\gamma_0^2+r^2\Omega^2\sin^2(\theta)-1}}{\gamma_0-r^2\Omega^2\sin^2(\theta)\sqrt{\gamma_0^2+r^2\Omega^2\sin^2(\theta)-1}} r\Omega\sin(\theta), \tag{20}$$

and its maximal value is reached at $r \approx 1.27\gamma_0/\Omega$ and equals

$$\beta_{\phi,\max} \approx 0.3/\gamma_0. \tag{21}$$

The angle of motion with respect to the radial direction, $\tan\chi = \beta_\phi/\beta_r$ always remains small (Figure 5).

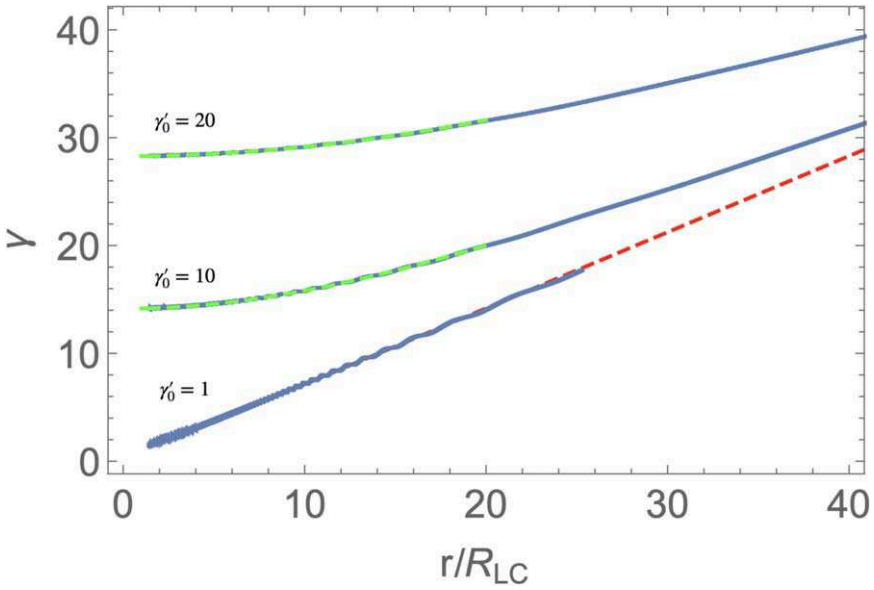

Figure 6. Direct integration of particle trajectories for the Lorentz factor of parallel motion $\gamma_0{}' = 1, 10, 20$, $\theta = \pi/4$ (solid lines). The $\gamma_0{}' = 1$ reproduces Michel's solution $\gamma = \sqrt{1 + r^2/2}$ (red-dashed line). Green dashed lines: analytical solutions (Equation (18)). In the simulations, the magnetic field at the light cylinder satisfies $\omega_B = 10^4\Omega$.

We also note simple relations in terms of proper time τ (for $\theta = \pi/2$).

$$\frac{dr}{d\tau} = \gamma\frac{dr}{dt} = \sqrt{\gamma_0^2 + r^2\Omega^2 - 1}$$
$$\frac{d^2r}{d\tau^2} = r\Omega^2. \tag{22}$$

Equation (22) has the solution

$$\Omega r(\tau) = \gamma_0 \sinh(\tau\Omega) + \cosh(\tau\Omega)$$
$$r'(\tau) = \gamma_0 \cosh(\tau\Omega) + \sinh(\tau\Omega) \tag{23}$$

(using $r(0) = 1/\Omega$ and $r'(0) = \gamma_0$). In proper time the Lorentz factor doubles approximately in $\tau \sim 1/\Omega$. This result is consistent with doubling in observer time in $t \sim \gamma_0/\Omega$, at a distance of $r \sim \gamma_0 R_{\rm LC}$.

3.3. Schwarzschild Black Hole, a = 0

The metric tensor is now

$$G_{00} = \alpha^2 - \sin^2\theta r^2\Omega^2 = G^{rr}$$
$$G_{0r} = -\sin^2\theta\frac{r^2\Omega^2}{\alpha^2} = G^{0r}$$
$$G_{rr} = \alpha^{-2} + \sin^2\theta\frac{r^2\Omega^2}{\alpha^4} = G^{00}$$
$$||G|| = -1 \tag{24}$$

(a factor of -1 is explicitly included in the definition of the 0–0 component of the metric).

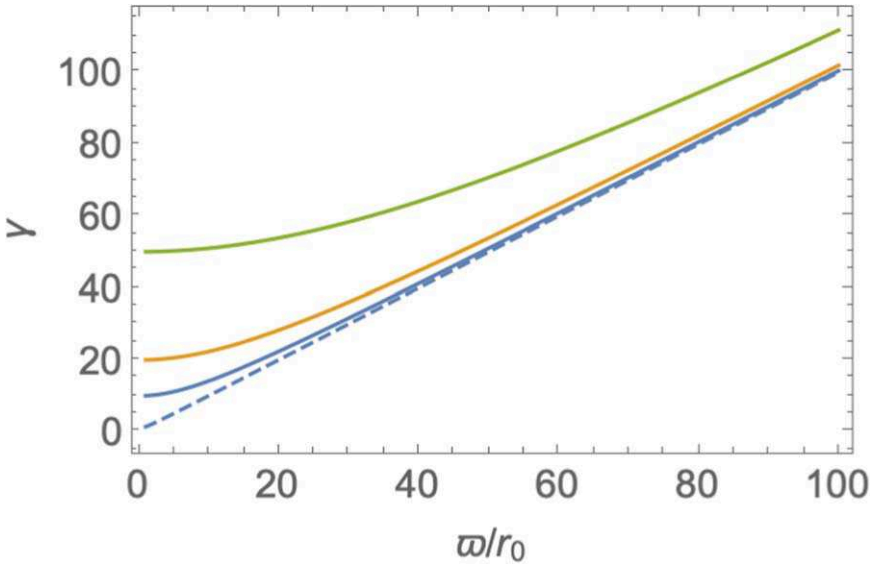

Figure 7. Lorentz factors of particles moving along parabolic spiral for different $\gamma_0 = 10, 20, 50$ (bottom to top curves). The dashed line denotes the Michel solution.

The Christoffel symbols evaluate to

$$\begin{aligned}
\Gamma^0_{00} &= -\frac{\Omega^2 \sin^2(\theta)(M - r^3\Omega^2 \sin^2(\theta))}{\alpha^2} \\
\Gamma^0_{0r} &= -\frac{(r^3\Omega^2 \sin^2(\theta) - M)(\alpha^2 + r^2\Omega^2 \sin^2(\theta))}{\alpha^4 r^2} \\
\Gamma^0_{rr} &= \frac{\Omega^2 \sin^2(\theta)(-5M + r^3\Omega^2 \sin^2(\theta) + 2r)}{\alpha^6} \\
\Gamma^r_{rr} &= \frac{\Omega^2 \sin^2(\theta)(-3M + r^3\Omega^2 \sin^2(\theta) + r)}{\alpha^4} + \frac{2M^2}{r^3\alpha^4} - \frac{M}{\alpha^4 r^2} \\
\Gamma^r_{0r} &= \frac{\Omega^2 \sin^2(\theta)(M - r^3\Omega^2 \sin^2(\theta))}{\alpha^2} \\
\Gamma^r_{00} &= \frac{(r^3\Omega^2 \sin^2(\theta) - M)(r^3\Omega^2 \sin^2(\theta) - \alpha^2 r)}{r^3}.
\end{aligned} \tag{25}$$

The radial velocity is now

$$\begin{aligned}
\beta_r &= \alpha^2 \frac{\alpha^2 - \sin^2\theta r^2\Omega^2}{\frac{\alpha^2\gamma_0}{\sqrt{\gamma_0^2 + \sin^2\theta r^2\Omega^2 - \alpha^2}} - \sin^2\theta r^2\Omega^2} \\
&= \begin{cases} \alpha^2\left(1 - \dfrac{\alpha^2}{2\gamma_0^2}\right), & \gamma_0 \gg r\Omega\sin\theta \\ \alpha^2\left(1 - \dfrac{1}{\sin^2\theta r^2\Omega^2} + \dfrac{\gamma_0}{\alpha^2 \sin^3\theta r^3\Omega^3}\right), & r \to \infty \end{cases}.
\end{aligned} \tag{26}$$

Factors of α^2 in front are just relativistic coordinate time dilation for a particle moving in the gravitational field.

3.4. Kerr Black Hole

In the equatorial plane we find

$$\beta_r = \frac{\alpha\sqrt{\Delta}\,\Delta_1(r(\alpha^2 - \Delta_1\Omega^2) - 4aM^2\Omega)}{\gamma_0\sqrt{\frac{r(4a^2\Delta_1 M^4 r^2(\alpha^2 + \Delta_1\Omega^2) - 16a^3\Delta_1 M^6 r\Omega + 16a^4M^8 - 8a\alpha^2\Delta_1^2 M^2 r^3\Omega + \alpha^4\Delta_1^2 r^4)}{4aM^2\Omega + r(-\alpha^2 + \gamma_0^2 + \Delta_1\Omega^2)}} + 4a^2M^4 - \Delta_1^2 r^2\Omega^2}}. \tag{27}$$

For $r \to \infty$, we find

$$\beta_r = \alpha^2 - \frac{1 - a^2M^2\Omega^2/2}{r^2\Omega^2} + \frac{\gamma_0 + 4M\Omega(1 - aM\Omega/2)}{r^3\Omega^3}. \tag{28}$$

It is understood that the solutions above involve both the kinematic effects of time dilation (e.g., a factor of α in front for the Schwarzschild case), as well as effects of centrifugal acceleration.

In conclusion, in all cases, a particle moves radially with $\gamma \approx \gamma_0$ until $r\Omega \sim \gamma_0$. After that, the wind acceleration takes over with $\gamma \sim r\Omega$.

3.5. Spiral with Arbitrary Radial Step

The radial step of a magnetic spiral (denoted below $\equiv c/\Omega_1$) may be different from c/Ω, e.g., the field may be affected by plasma inertia. For example, it is expected that inertial effects will make the spiral more tightly bound, with larger $d\phi'$ for a given dr; hence, $\Omega_1 \geqslant \Omega$. Equivalently, if the fast mode propagates with $\beta_s \leqslant 1$, in Equation (3),

$$\begin{aligned} &\beta_F \to \beta_s\beta_F \\ &\Omega_1 = \frac{\Omega}{\beta_s} \geqslant \Omega. \end{aligned} \tag{29}$$

Most importantly, the radial velocity of fast mode's propagation may change with radius depending on local plasma parameters. In this case, the shape of the spiral is non-Archimedean. In our notations, this implies radial dependence of the radial step: $\Omega_1(r)$.

Corresponding relations are fairly compact in the Schwarzschild metric. Using

$$\begin{aligned} &d\phi \to d\phi' - \Omega dt \\ &d\phi' \to -\frac{\Omega_1}{\alpha^2}dr \end{aligned} \tag{30}$$

(instead of the corresponding relations (Equation (5)) with $\Omega_1 = \Omega$), we find

$$\begin{aligned} \beta_r &= \frac{\alpha^2(\alpha^2 - r^2\Omega^2)}{\frac{\alpha\gamma_0\sqrt{\alpha^2 + r^2(\Omega_1^2 - \Omega^2)}}{\sqrt{-\alpha^2 + \gamma_0^2 + r^2\Omega^2}} - r^2\Omega\Omega_1} \\ &= \begin{cases} \alpha^2\left(\dfrac{\alpha^2 - r^2\Omega^2}{\alpha\sqrt{\alpha^2 + r^2(\Omega_1^2 - \Omega^2)} - r^2\Omega\Omega_1}\right), & \gamma_0 \gg r\Omega \\ \alpha^2\left(\dfrac{\Omega}{\Omega_1} - \dfrac{(\Omega_1 - \gamma_0\sqrt{\Omega_1^2 - \Omega^2})}{\alpha^2 r^2\Omega_1^2\Omega}\right), & r \to \infty \end{cases}. \end{aligned} \tag{31}$$

For flat space,

$$\beta_r = \frac{1 - r^2\Omega^2}{\frac{\gamma_0\sqrt{1 + r^2(\Omega_1^2 - \Omega^2)}}{\sqrt{\gamma_0^2 + r^2\Omega^2 - 1}} - r^2\Omega\Omega_1} = \begin{cases} \dfrac{1 - r^2\Omega^2}{\sqrt{1 + r^2(\Omega_1^2 - \Omega^2)} - r^2\Omega\Omega_1}\left(1 - \dfrac{(1 - r^2\Omega^2)\sqrt{r^2(\Omega_1^2 - \Omega^2) + 1}}{2\gamma_0^2(\sqrt{r^2(\Omega_1^2 - \Omega^2) + 1} - r^2\Omega\Omega_1)}\right), & \gamma_0 \gg \Omega r \\ \dfrac{\Omega}{\Omega_1} - \dfrac{(\Omega_1 - \gamma_0\sqrt{\Omega_1^2 - \Omega^2})}{r^2\Omega_1^2\Omega}, & r \to \infty \end{cases}. \tag{32}$$

Importantly, in the above relations, the function $\Omega_1(r)$ is arbitrary, limited only by the condition $\Omega_1 \geqslant \Omega$. (So that a radial step per rotation can be smaller or equal to the light cylinder.)

For given Ω and Ω_1 the toroidal velocity is

$$\beta_\phi = r\Omega\left(1 - \frac{\Omega_1}{\Omega}\beta_r\right). \tag{33}$$

Note that here Ω_1 may depend on radius r.

On physical grounds, we expect $\Omega_1 \approx \Omega$. In other words, the fast mode is nearly relativistic and plasma is nearly force-free. This is the intrinsic assumption of the model. For example, if $\Omega_1 = (1 + \delta_\Omega)\Omega$, $\delta_\Omega \ll 1$, then

$$\beta_\phi = r\Omega(1 - \beta_r + \delta_\Omega). \tag{34}$$

Thus, for an Archimedean spiral with the radial step $1/\Omega$, a particle slightly overtakes the rotation pattern with the rate of $\sim r\Omega(1 - \beta_r) \ll r\Omega$, while for $1 - \beta_r \ll \delta_\Omega$ a particle lags behind.

Thus, azimuthal velocity is small right from the light cylinder. The maximal toroidal velocity is $\sim 1/\gamma_0$, or $\sim \delta_\Omega$.

4. Numerical Test

We have developed a Boris-based pusher (Boris & Roberts 1969; Birdsall & Langdon 1991). We verify the analytical results with direct integration, as we discuss below.

For the Michel solution, consider a particle that in the wind frame (boosted by $\beta_{\rm EM}$ from the lab frame) moves with Lorentz factor $\gamma_0{}'$ (prime indicates Lorentz factor measured in the flow frame). Using electromagnetic velocity (Equation (1)) and Lorentz transformations, we find the momentum in the lab frame $p_\parallel$ of

$$p_\parallel = \left\{ \frac{\beta_0{}'\gamma_0{}' + (\gamma_0{}' - 1) r^2 \sin^2\theta\Omega^2}{\sqrt{1 + r^2\sin^2\theta\Omega^2}}, 0, \frac{(\sqrt{1 - \beta_0{}'} - \sqrt{\beta_0{}' + 1})\, r\Omega \sin(\theta)}{\sqrt{\beta_0{}' + 1}\sqrt{1 + r^2\Omega^2\sin^2(\theta)}} \right\}. \tag{35}$$

The momentum $p_\parallel$ is that of a particle that is sliding along the local magnetic field with Lorentz factor $\gamma_0{}'$ as measured in the frame associated with $\beta_{\rm EM}$ (where the electric field is zero). This is not a radial dependence, only a transformation at a given radius.

The total Lorentz factor is

$$\gamma = \gamma_0{}'\sqrt{1 + \sin^2\theta r^2\Omega^2} = \sqrt{2}\gamma_0{}', \tag{36}$$

a combination of parallel motion and orthogonal E-cross-B drift. The final relation in Equation (36) applies to the light cylinder.

In Figure 6 we compare the analytical results (Equation (18)) and numerical integration—they are in excellent agreement.

5. Jet in M87

5.1. Particle Dynamics in a Parabolic Magnetic Field

In our model collimation is completely separated from acceleration in the vicinity of the light cylinder. To demonstrate this, let us choose prescribed collimated flow along the parabolic flux surfaces

$$r(1 - \cos\theta) = \text{const}. \tag{37}$$

In this case, it is more convenient to work in cylindrical coordinates. The flux surface is then given by

$$z = \frac{\varpi^2 - r_0^2}{2r_0} \tag{38}$$

(ϖ is a cylindrical radial coordinate, r_0 is a parameter that marks a particular flux surface).

In the metric tensor we first change to the rotating frame, $d\phi \to d\phi' - \Omega dt$, add the parabolic constraint $dz \to (\varpi/r_0)d\varpi$, and add a spiral step

$$\begin{aligned} d\phi' &= \Omega dl \\ dl &= \sqrt{1 + \varpi^2/r_0^2}\, d\varpi. \end{aligned} \tag{39}$$

At each location the velocity in the $\{\varpi, \phi, z\}$ coordinates is

$$\left\{ \beta_\varpi, \Omega\varpi\left(1 - \sqrt{1 + \frac{\varpi^2}{\varpi_0^2}}\,\beta_\varpi\right), \frac{\varpi\beta_\varpi}{\varpi_0} \right\}. \tag{40}$$

The metric tensor in this case is

$$G_{00} = 1 - \Omega^2\varpi^2$$
$$G_{0\varpi} = \Omega^2\varpi^2\sqrt{1 + \frac{\varpi^2}{\varpi_0^2}}$$
$$G_{\varpi\varpi} = \left(1 + \frac{\varpi^2}{\varpi_0^2}\right)\Omega^2\varpi^2. \tag{41}$$

Following our procedure we find

$$\beta_\varpi = \frac{1 - (2\varpi - r_0)r_0\Omega^2}{\frac{\gamma_0}{\sqrt{\frac{(2\varpi - r_0)(\gamma_0^2 + (2\varpi - r_0)r_0\Omega^2 - 1)}{(2\varpi - r_0)r_0^2\Omega^2 - 2\varpi}}} - (2\varpi - r_0)r_0\Omega^2}. \tag{42}$$

The resulting acceleration differs little from the case of conical flux surfaces of the Michel solution (Figure 7).

5.2. Emission Maps

As we demonstrated above, particles injected from the black hole magnetosphere stream nearly along the magnetic flux surfaces—either conical for monopolar fields, parabolically, or more generally, along any given flux surface. The toroidal velocity remains small.

For a given shape of the magnetic flux surface (and some prescription for emissivity) we can then calculate the expected emission map. For the monopolar magnetosphere, any emission by relativistic radially moving particles will be centered on the source, the black hole.

Even for curved flux surfaces, particles move with constant Lorentz factor almost purely along the flux surfaces, with minimal v_ϕ. For high injection Lorentz factors the emission will be dominated by the flow points when particle motion is aligned with the line of sight.

For example, for parabolical flux surfaces (Blandford & Znajek 1977), also Equation (37), neglecting GR contribution, the line of sight can be parallel to a given flux surface emanating from the magnetosphere only if the line of sight is $\theta_{\rm ob} \leqslant \pi/4$. For smaller $\theta_{\rm ob}$, for a given flux surface parameterized by r_0 the tangent point is

$$\varpi_t = r_0 \cot\theta_{\rm ob}$$
$$z_t = (\cot^2\theta_{\rm ob} - 1)\frac{r_0}{2}. \tag{43}$$

Choosing axis x_s on the plane of the sky along the projection of the spin of the black hole on the plane of the sky, the tangent point projects to

$$x_s = \frac{r_0}{2\sin\theta_{\rm ob}}$$
$$y_s = 0. \tag{44}$$

Since the observed pattern is dominated by Lorentz boost, to calculate the images we employ the following procedure (see Figures 8 and 9):

1. Given the velocity (Equations (40)–(42)) we calculate the local Doppler factor δ. In fact, since toroidal velocity is small, one can use just the shape of the flux surface to find the local direction of the flow.
2. We scale the local density (somewhat arbitrary) as $1/r^2$, the total spherical distance to the black hole.
3. Local emissivity is parameterized as

$$j \propto \frac{\delta^3}{r^2}. \tag{45}$$

4. Emissivity is integrated along the line of sight.

In Figure 10 we plot slices of the Doppler factor in the two orthogonal planes. Expected brightness maps are plotted in Figures 11–13. All images, for any surface parameter, r_0, are spine brightened. Hence, any combination will be spine brightened as well.

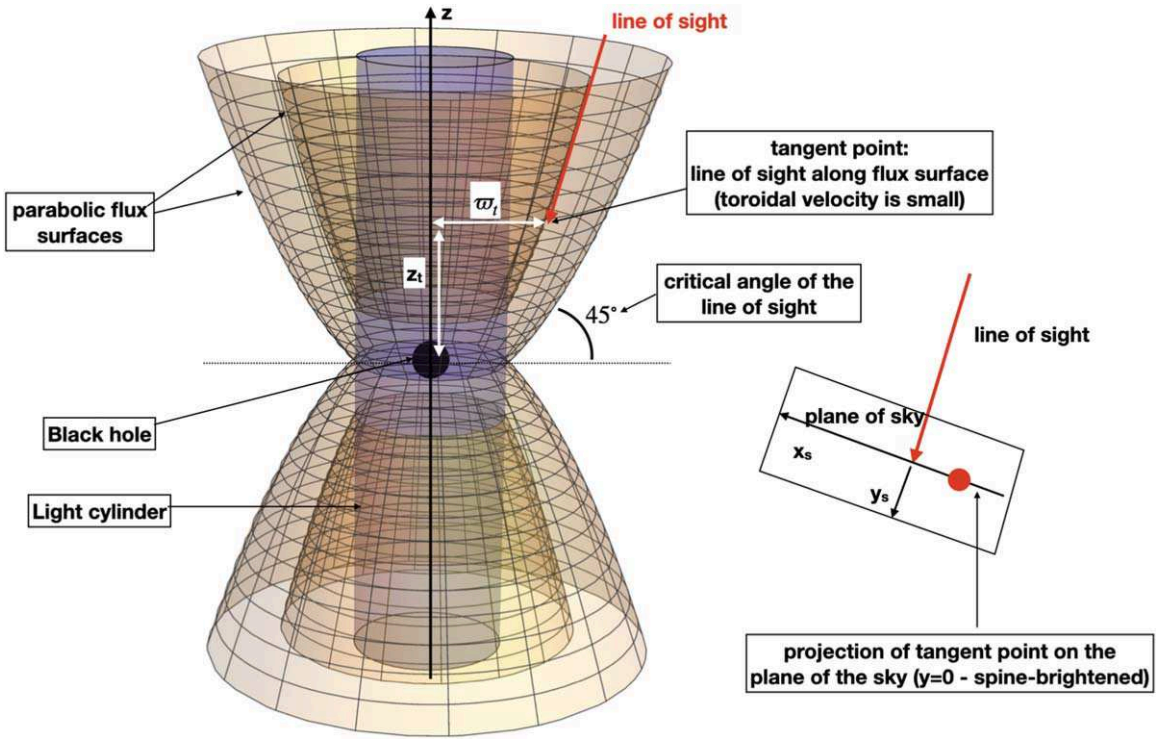

Figure 8. 3D rendering of the parabolic magnetosphere. The vertical cylinder is the light cylinder. The insert on the right shows the sky image for a particular chosen line of sight. Due to high Doppler boosting the brightness peaks on the y-axis—the spine.

Finally, we conciliate emission from a possible current sheet outside of the light cylinder (Comisso & Asenjo 2021), by integrating the flux parameter r_0 from 1 to 2. The resulting structure is more elongated, and more extended sideway, but is still spine brightened (Figure 14).

5.3. Conclusion: Morphology of M87 Jet and the BZ Mechanism

Our results show a universal property of the resolved BZ flow with large parallel (to the local magnetic field) momentum of emitting particles: all images are spine brightened, agreeing with what was observed. No special prescription for emissivity as a function of the flux function parameter r_0 can change that: they are all spine brightened. The assumption of parabolical flux surfaces is, naturally, an analytic approximation, yet the universality of the result—spine-brightened profile—ensures that it will be applicable to more general cases.

We then conclude that the BZ mechanism is responsible for the M87 jet, at least in its pure form. By the BZ mechanism, we understand the generation of a collimated relativistic jet. The relativistic $e^{\pm}$ we describe does extract energy from the spin of the black hole.

The BZ mechanism can still be operational—and, e.g., responsible for the bright core in the images of M87 in case of purely radial outflow at small r, but it does not drive the observed jet. Another possibility is that the sheath is slowed down by the interaction with the disk corona—while the core remains relativistic, with emission beamed away. This would correspond to emission coming only from small r_0, top rows in Figures 11 and 12—it is still spine brightened, but shows only in the small part of the image.

In contrast, disk-produced outflows (Blandford & Payne 1982) start nonrelativistically. The extended structure observed in M87 is thus inconsistent with the magnetosphere-produced jet, but is consistent with the disk-produced jets.

On larger scales, of the order of parsecs, in the grand spiral paradigm of a jet moving with a Lorentz factor of approximately a few (Lyutikov et al. 2005), the edge-brightened jet is actually expected on theoretical grounds (e.g., Figure 1 of Clausen-Brown et al. 2011). In addition, asymmetries across the jet in intensity, polarization, and spectral index maps are expected.

5.4. Plasma Dynamics and Pair Production in Force-free and PIC Simulations

Two approaches are commonly used to study relativistic winds and jets: force-free simulation (e.g., Spitkovsky 2006) and PIC simulations (e.g., Chen & Beloborodov 2014; Philippov et al. 2015; Crinquand et al. 2020; Hakobyan et al. 2023; Ripperda et al. 2022).

In an ideal force-free simulation, the velocity along the field is not defined in principle. (Inclusion of resistivity in the force-free approach requires some choice of parallel velocity (Lyutikov 2003; Gruzinov 2007.) Thus, the effects discussed here are completely missed in force-free simulation.

In the case of PICs, the effects of the initial large injection Lorentz factor are missed by choice (see though Crinquand et al. 2020). To simulate pair production in PICs typically some kind of prescription is employed: either a density floor or a condition on the value

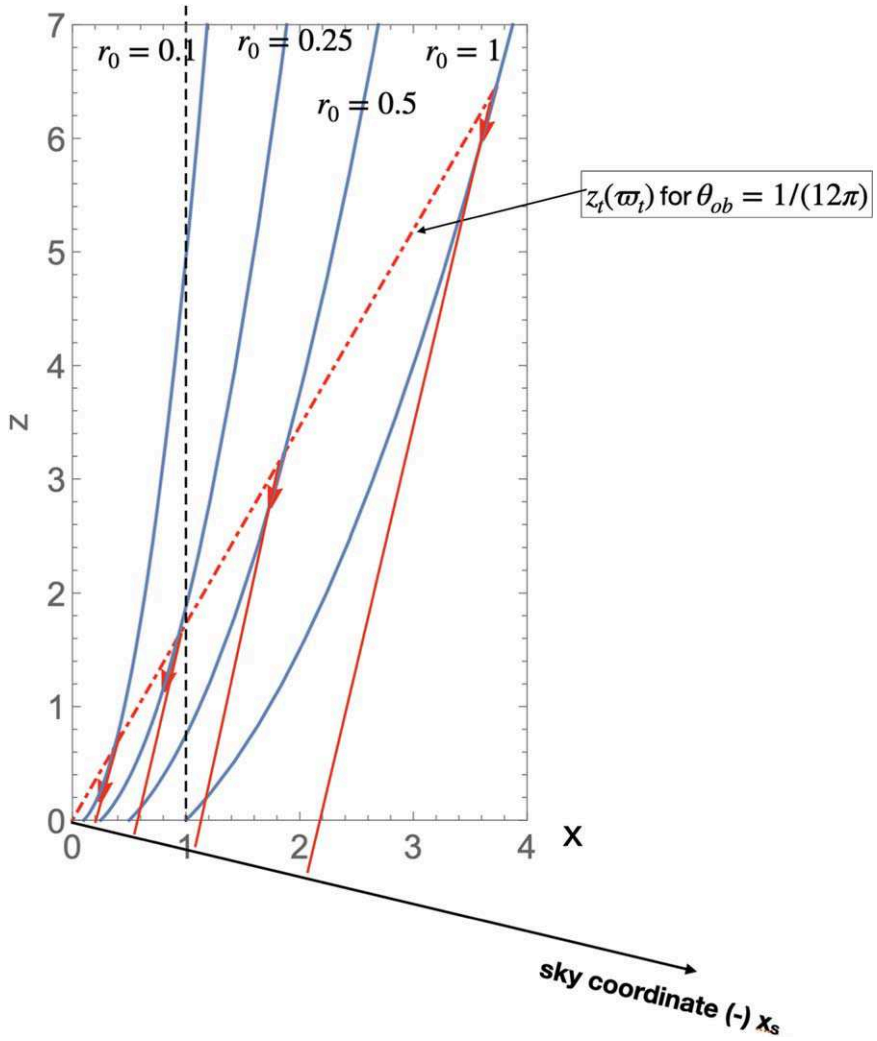

Figure 9. Parabolic magnetosphere and the lines of sight, $x - z$ cut. Solid lines indicate the magnetic flux surface for $r_0 = 0.1, 0.25, 0.5, 1$. Red arrows start at points where the local line of sight is along the flux surface (hence the maximal Doppler factor). Red-dashed line, Equation (44)—location of all such points. In this example, $\theta_{ob} = \pi/12$. Coordinates are normalized to light cylinder radius.

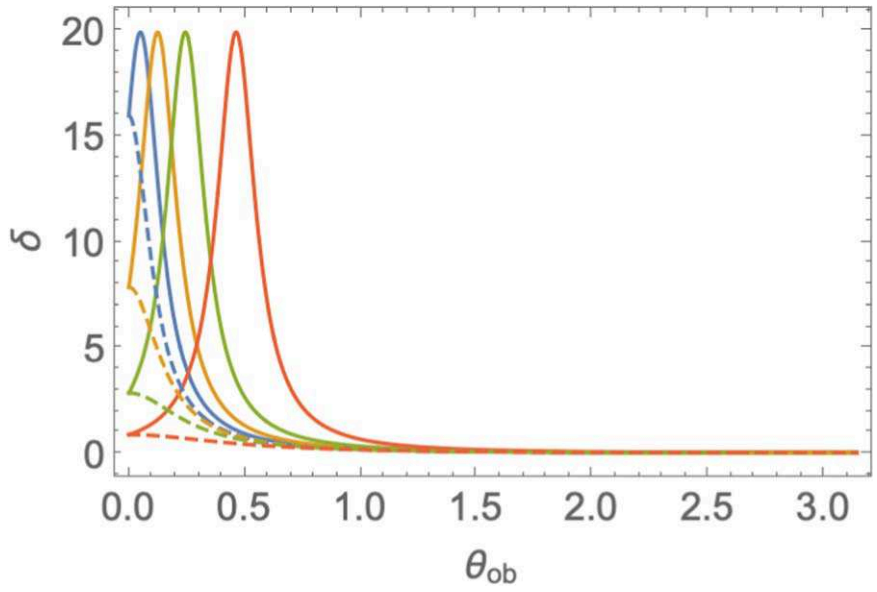

Figure 10. Doppler factor as a function of the observer angle θ_{ob} at $r = 2$. Slices are in the line-of-sight black hole spin plane (solid lines) and in the orthogonal plane (dashed lines). Peaks in δ correspond to angles when the line of sight is tangential to the flux surface. Here and for the images below $\gamma_0 = 10$.

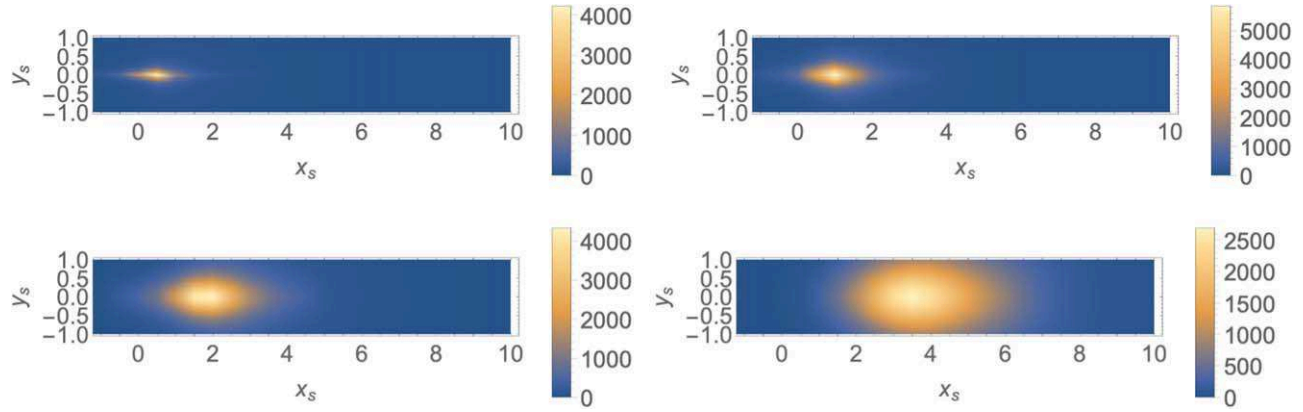

Figure 11. Image maps for $r_0 = 0.1, 0.25, 0.5, 1$, $\theta_{ob} = \pi/12$. The axes correspond to projected distances measured in terms of the light cylinder radius.

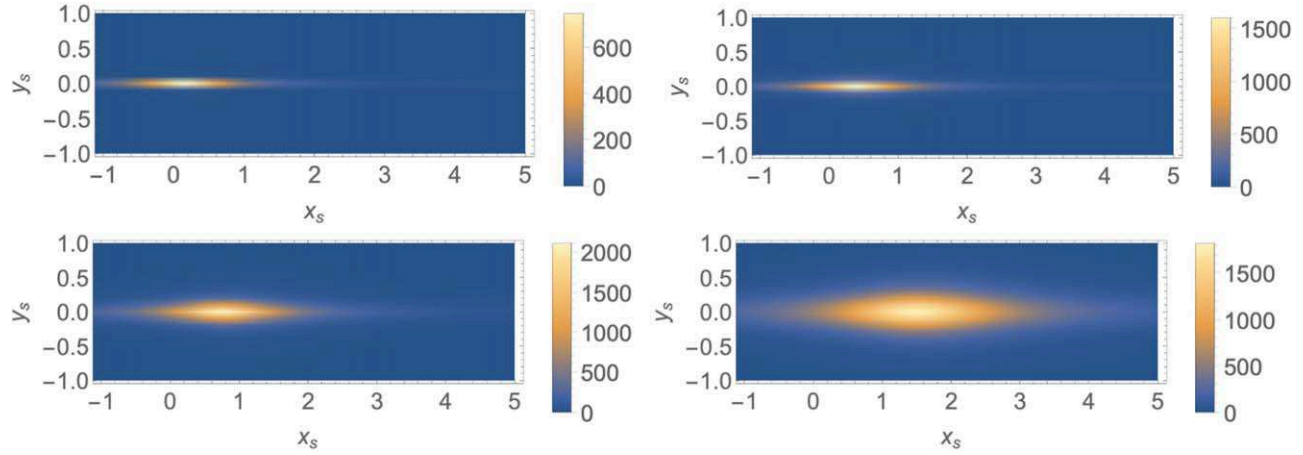

Figure 12. Image maps for $r_0 = 0.1, 0.25, 0.5, 1$, $\theta_{ob} = \pi/6$.

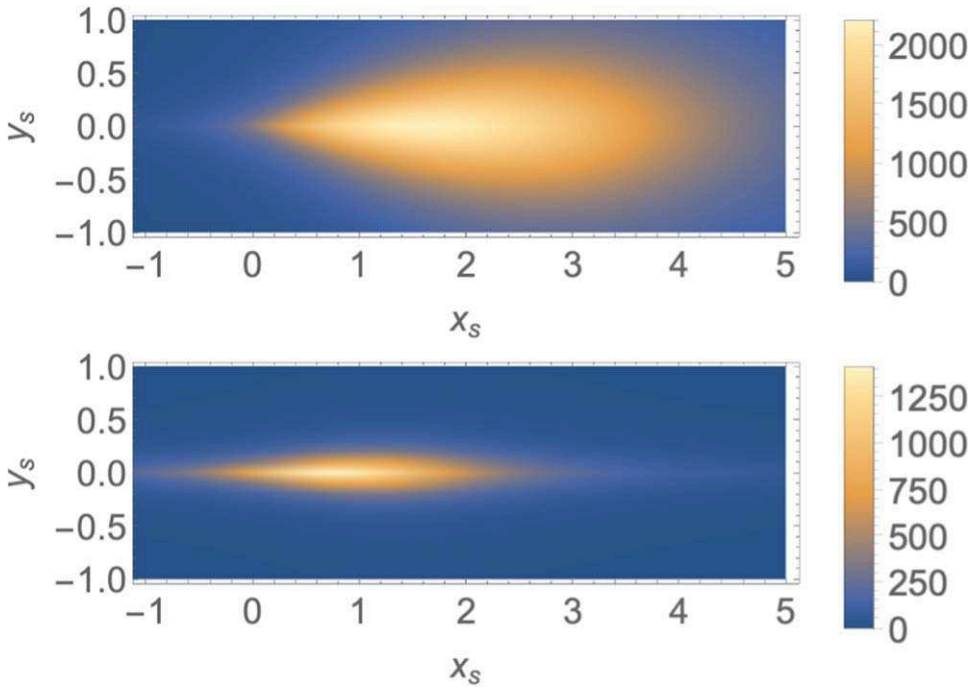

Figure 13. Image maps integrated over $0 \leqslant r_0 \leqslant 1$ for $\theta_{ob} = \pi/12$ (top panel) and $\theta_{ob} = \pi/6$ (bottom panel). Larger r_0 corresponds to flux surfaces not emanating from the magnetosphere.

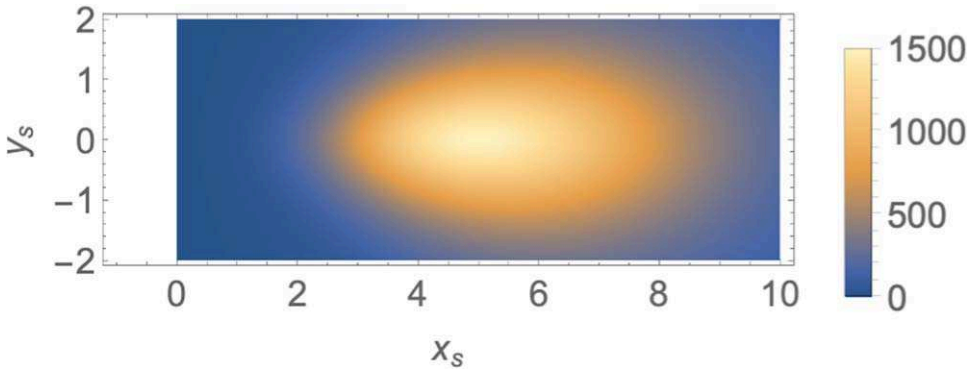

Figure 14. Emission pattern from the outside current sheet, $1 \leqslant r_0 \leqslant 2$.

of the local electric field. Acceding to a given prescription pairs are added *at rest* (except in Crinquand et al. 2020). Instead, they should be added with large Lorentz factors. If the number of added pairs is comparable to the initial one, the resulting structure of the magnetosphere will be drastically different.

Our results have implications for PIC simulations (that the newly born $e^{\pm}$ pairs should injected with a large initial Lorentz factor), and interpretation of the images of black holes by the Event Horizon Telescope.

This is a qualitatively different setup from what the conventional black hole acceleration models assume. Jets start fast, with a Lorentz factor $\gg 1$. At first, they carry a small power. Only later on does the magnetic field acceleration take over.

6. Discussion

We demonstrate that outflows produced within magnetospheres of neutron stars and black holes start relativistically right from within the light cylinder. To produce jets the overall magnetic field just needs to collimate the outflow—acceleration is already achieved by injection. For highly magnetized flows with $\sigma \gg 1$ the kinetic luminosity of the jet is $L_k \sim L_{\rm P}/\sigma \leqslant L_{\rm P}$, when $L_{\rm P}$ is the Poynting power, but the jet is already relativistic. It can be further accelerated by the magnetic forces beyond $r\Omega \sim \gamma_0$.

Any signal produced by radially moving particles with $\gamma \gg 1$ will be centered on the source. For parabolic flux surfaces, we calculated the expected images—they are all spin brightened, in agreement with observations of the M87 jet. We then conclude that the M87 jet can be produced with the black hole magnetosphere by the BZ mechanism.

Finally, we point out that in PIC simulations pairs must be injected relativistically—this will change the overall structure of both pulsar and black hole magnetospheres.

Acknowledgments

This work had been supported by NASA grant 80NSSC18K064 and NSF grants 1903332 and 1908590. We would like to thank Nahum Arav, Maxim Barkov, Vasily Beskin, Ioannis Contopoulos, Hayk Hakobyan, Sergey Komissarov, Mikhlail Medvedev, Frank Rieger, Markek Sikora, and Elena Nokhrina for comments, and the organizers of the IAU conference "Black Hole Winds at all Scales" for hospitality.

Data Availability

The data underlying this article will be shared on reasonable request to the corresponding author.

Appendix A
Constrained Motion in Flat Space

Here we aim to re-derive the results for flat metrics using Lagrangian and Hamiltonian approaches for constrained motion in flat space.

Consider relativistic particles moving along a rotating spiral in cylindrical coordinates in flat space. One possible choice of relativistic Lagrangian is (Landau & Lifshitz 1975)

$$\mathcal{L} = -\sqrt{1 - \beta_\phi^2 - \beta_r^2} \tag{A1}$$

(see also Appendix B for an alternative choice).

The field lines of the Michel solution are given as a parametric curve in x–y–z coordinates (at any moment t)

$$\begin{aligned} &\mathcal{C}\colon \{r\sin(\theta)\cos(\phi),\, r\sin(\theta)\sin(\phi),\, r\cos(\theta)\} \\ &\phi = (t - r)\Omega, \end{aligned} \tag{A2}$$

where spherical r is a parameter along the curve, Figure 15.

The total velocity (differentiating Equation (A2) with respect to time) is

$$\mathbf{v} = \beta_r \mathbf{e}_r + \sin\theta r\Omega(1 - \beta_r) e_\phi. \tag{A3}$$

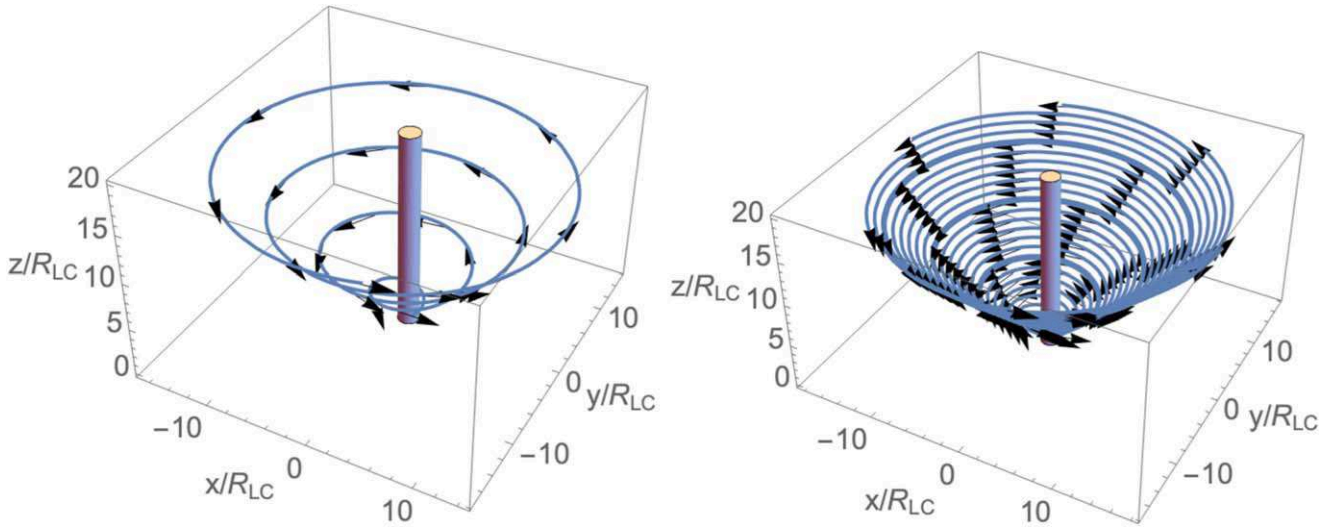

Figure 15. Field lines for Michel's solution.

The Lagrangian then becomes

$$\mathcal{L} = -\sqrt{1 - \beta_r^2 - \sin^2\theta r^2\Omega^2(1 - \beta_r)^2} \tag{A4}$$

($\theta = \pi/2$ is assumed below for simplicity).

The Lagrange equation for coordinate r with $\beta_r = \partial_t r$ is

$$\partial_r \mathcal{L} = \partial_t(\partial_{\beta_r}\mathcal{L}), \tag{A5}$$

which gives

$$\partial_t \beta_r = r\Omega^2(1 - \beta_r)^2(1 - r^2\Omega^2 + \beta_r(2 + r^2\Omega^2)). \tag{A6}$$

The solution satisfying $r(t = 0) = 1/\Omega$ is

$$t = r - \frac{1}{\Omega} + \frac{\log\left(\frac{(\gamma_0^2 - 1)(r\Omega - 1)(\sqrt{\gamma_0^2 + r^2\Omega^2 - 1} + \gamma_0 r\Omega)}{\gamma_0^2(r\Omega + 1)(\gamma_0 r\Omega - \sqrt{\gamma_0^2 + r^2\Omega^2 - 1})}\right)}{2\Omega} \tag{A7}$$

where the integration constant γ_0 was chosen to match Equation (17). Differentiating Equation (A7) with respect to time we recover Equation (17).

As a check, let us repeat the above derivation using the Hamiltonian approach. Given the Lagrangian (Equation (A4)) we can find canonical momentum P_r and Hamiltonian

$$P_r = \partial_{\beta_r}\mathcal{L} = \frac{\beta_r - r^2\Omega^2(1 - \beta_r)}{\sqrt{1 - \beta_r^2 - r^2\Omega^2(1 - \beta_r)^2}}$$
$$\mathcal{H} = \beta_r P_r - \mathcal{L} = \frac{r^2\Omega^2 P_r + \sqrt{P_r^2 + r^2\Omega^2 + 1}}{r^2\Omega^2 + 1}. \tag{A8}$$

The canonical equations are then

$$\beta_r = \partial_t r = \partial_{P_r}\mathcal{H} = \frac{r^2\Omega^2}{1 + r^2\Omega^2} + \frac{P_r}{(1 + r^2\Omega^2)\sqrt{1 + P_r^2 + (r\Omega)^2}}$$
$$\partial_t P_r = -\partial_r \mathcal{H} = \frac{r\Omega^2(-2P_r\sqrt{P_r^2 + r^2\Omega^2 + 1} + 2P_r^2 + r^2\Omega^2 + 1)}{(r^2\Omega^2 + 1)^2\sqrt{P_r^2 + r^2\Omega^2 + 1}}. \tag{A9}$$

Equating $\mathcal{H} = \gamma_0$ we find

$$P_r = \frac{\gamma_0 r^2\Omega^2 + \sqrt{\gamma_0^2 + r^2\Omega^2 - 1}}{1 - r^2\Omega^2}. \tag{A10}$$

Using Equation (A10) in the expression for the velocity Equation (A9) we recover Equation (17).

The Lagrangian approach requires integration of the equations of motion and allows one to find $r(t)$, while the more simple Hamilton–Jacobi approach, which involves only algebraic relations, gives only $\beta_r(r)$. This is sufficient for our application.

Appendix B
Using Another Lagrangian Approach in the Schwarzschild Metric

Let us next extend the results of Appendix A to the Schwarzschild metric using a somewhat different approach. We are interested in getting the radial speed of the particle along the string (i.e., on the (1+1)-D manifold). The alternative choice of Lagrangian is

$$\mathcal{L}(\dot{t}, \dot{r}, r) = \frac{1}{2}[-G_{00}\,\dot{t}^2 + G_{rr}\,\dot{r}^2 + 2G_{0r}\,\dot{t}\dot{r}], \qquad \dot{x} = \frac{dx}{d\tau}. \tag{B1}$$

From the symmetry of the Lagrangian in the t coordinate, we use the Euler–Lagrange equation to get

$$\dot{t} = \frac{G_{0r}\,\dot{r} + E}{G_{00}}, \qquad G_{00} \neq 0, \tag{B2}$$

where E is a constant of motion. It is generally different from γ_0 —different choices of the Lagrangian result in different integration constants; the exact relations between different constants are typically complicated.

For timelike trajectories,

$$\mathcal{L}(\dot{r}, r) = \frac{1}{2}\left[\left(G_{rr} + \frac{G_{0r}^2}{G_{00}}\right)\dot{r}^2 - \frac{E^2}{G_{00}}\right] = -\frac{1}{2}. \tag{B3}$$

The speed of the coordinate r with respect to the proper time (the time measured by the particle that is constrained to move along the string) is

$$\dot{r} = \pm\sqrt{\frac{E^2 - G_{00}}{G_{0r}^2 + G_{00}\,G_{rr}}}. \tag{B4}$$

The sign here determines the direction of motion: either toward or away from the black hole. The speed of the coordinate r with respect to the coordinate t is

$$\beta_r = \frac{dr}{dt} = \frac{\dot{r}}{\dot{t}} \overset{(B2)}{=} G_{00}\left(G_{0r} + \frac{E}{\dot{r}}\right)^{-1} = G_{00}\left(G_{0r} \pm E\sqrt{\frac{G_{0r}^2 + G_{00}\,G_{rr}}{E^2 - G_{00}}}\right)^{-1}. \tag{B5}$$

This recovers Equation (14), obtained by the Hamilton–Jacobi approach.

Consider rotating magnetosphere in Schwarzschild metric. We use the following convention:

$$G_{00} = \alpha^2 - r^2\Omega^2, \qquad G_{rr} = \frac{1}{\alpha^2} + \frac{r^2\Omega^2}{\alpha^4}, \qquad G_{0r} = -\frac{r^2\Omega^2}{\alpha^2}. \tag{B6}$$

The Lagrangian is then

$$\mathcal{L} = \frac{1}{2}\left(-\alpha^2\left(1 - \frac{r^2\Omega^2}{\alpha^2}\right)\dot{t}^2 + \frac{1}{\alpha^2}\left(1 + \frac{r^2\Omega^2}{\alpha^2}\right)\times\ \dot{r}^2 - 2\frac{r^2\Omega^2}{\alpha^2}\,\dot{t}\dot{r}\right). \tag{B7}$$

Between the two light cylinders, the constant of motion is

$$E = (\alpha^2 - r^2\Omega^2)\dot{t} + \frac{r^2\Omega^2}{\alpha^2}\dot{r}. \tag{B8}$$

We then get $\dot{r}$ by substituting in Equation (B4) or by solving the quadratic Equation (B7) using $G_{00}G_{rr} + G_{0r}^2 = 1$ (in our case):

$$\dot{r} = \frac{-G_{0r}\dot{t} \pm \sqrt{\dot{t}^2 - G_{rr}}}{G_{rr}}. \tag{B9}$$

Eliminating $\dot{t}$ with Equation (B8),

$$\dot{t} = \frac{\alpha^2 E - r^2\Omega^2 \dot{r}}{\alpha^2(\alpha^2 - r^2\Omega^2)}, \tag{B10}$$

we find the Lagrangian and Hamiltonian

$$\mathcal{L} = \frac{\dot{r}^2 - E^2}{2(\alpha^2 - r^2\Omega^2)},$$
$$\mathcal{H} = \dot{r}\partial_{\dot{r}}\mathcal{L} - \mathcal{L} = \frac{\dot{r}^2 + E^2}{2(\alpha^2 - r^2\Omega^2)}. \tag{B11}$$

We used ($\sqrt{2}$ times) the proper time to parameterize the Lagrangian in Equation (B7); thus, the Lagrangian has a constant value of $-1/2$ with this parameterization for timelike geodesics. Therefore, $\dot{r}$ is

$$\dot{r} = \pm\sqrt{r^2\Omega^2 + E^2 - \alpha^2}, \tag{B12}$$

consistent with Equation (22).

The radial velocity measured by the coordinate time of the observer is then

$$\beta_r = \frac{\dot{r}}{\dot{t}} = \frac{\alpha^2(\alpha^2 - r^2\Omega^2)}{\frac{\alpha^2 E}{\sqrt{r^2\Omega^2 + E^2 - \alpha^2}} - r^2\Omega^2}. \tag{B13}$$

The geodesic equation takes a nice form, i.e.,

$$\ddot{r} = \frac{1}{2}\frac{d}{dr}(\dot{r}^2) = r\Omega^2 - \frac{M}{r^2} \tag{B14}$$

(derivatives are with respect to proper time), which unites the cases of radial motion in Schwarzschild geometry (e.g., Misner et al. 1973 and Equation (22)).

We also note that one can get the same differential equation (for the case between the two light cylinders) by solving the classical mechanical problem of a particle with mass m constrained to move along a straight wire rotating with a constant angular speed Ω in the flat 2D plane, with the inclusion of a source of mass M at the center. The Lagrangian is ($\dot{r} = dr/dt$)

$$\mathcal{L} = \frac{1}{2}m(\dot{r}^2 + r^2\Omega^2) - U(r), \qquad U(r) = -m\frac{\mathrm{MG}}{r}. \tag{B15}$$

Appendix C
Limitations on the Angular Velocity of Field Lines

Transformation to the rotating Kerr metric has limitations (Lyutikov 2009): it is physical only for angular velocities smaller than ω_{ph}, the angular velocity of a photon orbit, defined by the conditions of circular rotation with the speed of light $g_{00} = 0$, $\partial_r g_{00} = 0$. This gives $-4a^2M + r(-3M + r)^2 = 0$ (Bardeen et al. 1972). For a given a and r, the transformation to the rotating Kerr metric becomes meaningless for ω higher than the angular velocity of a photon circular orbit,

$$\omega_{\rm ph} = \frac{1}{\mp|a| + 6M\cos\left(\frac{1}{3}\arccos(\mp|a|/M\right)}. \tag{C1}$$

The upper sign corresponds to prograde rotation. Particular values are $a = 0$, $r_{\rm ph} = 3M$, $\omega_{\rm ph} = 1/(3\sqrt{3}M)$ for the Schwarzschild black hole, $a = M$, $r_{\rm ph} = M$, $\omega_{\rm ph} = 1/(2M)$ for prograde and $a = -M$, $r_{\rm ph} = 4M$, and $\omega_{\rm ph} = 1/(7M)$ for retrograde photon orbits. For $1/(7M) < \omega < 1/(2M)$ this requires sufficiently high a, satisfying $\omega < 1/\left(a + 2\sqrt{2}M\left(1 + \cos\left(\frac{2}{3}\arccos(-\frac{a}{M})\right)\right)\right)^{3/2}$ (for $a = 0$ this requires $\omega < 1/(3\sqrt{3})$). For $\omega \to 1/(2M)$ both light cylinders merge on the black hole horizon at $a = M = r$. For higher ω, the transformation to the rotating frame becomes meaningless everywhere (Figure 16).

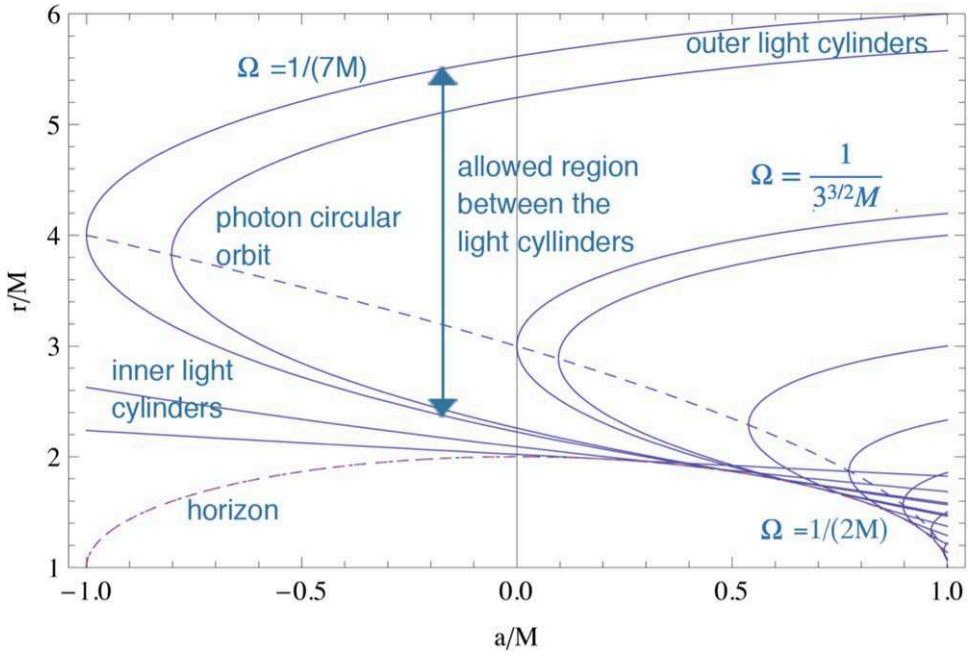

Figure 16. The locations of light cylinders for different ω as a function of a. The light cylinders always lie outside the horizon (dotted curve). For a given ω, the inner and outer light cylinders merge at the photon circular orbit (dashed line). The physically meaningful region lies in between the light cylinders, to the right of the light cylinders curve. For $\omega \to 0$, the inner light cylinder coincides with the ergosphere $r = 2M$. As ω increases, the outer light cylinder moves to smaller r; the radial location of the inner light cylinder is a complicated function of ω. For $\omega > 1/(7M)$ there is a region for sufficiently small a, for which the transformation to the rotating frame is unphysical. For high $\omega \to 1/(2M)$ and high $a > M/\sqrt{2}$, the inner light cylinder moves inside the ergosphere of a Kerr black hole. For $\omega > 1/(2M)$, the transformation to a rotating frame is unphysical everywhere. Adapted from Lyutikov (2009).

Appendix D
Kerr Black Hole Analysis

In this appendix, we calculate the velocity components relative to an observer at infinity and show that the radial component dominates in a few light cylinder radii; we also obtain the Lorentz factor of the speed relative to both fixed observers in spacetime and corotating observers with the field lines.

We consider a (2+1)-D manifold of the Kerr black hole with a constant θ. Then, we move to a (1+1)-D sub-manifold that is rotating with a constant angular speed Ω according to

$$d\phi = \Phi'(r)\, dr + \Omega\, dt \qquad \Phi'(r) = \frac{d\Phi(r)}{dr}. \tag{D1}$$

This means that a particle in this sub-manifold is constrained to move along a wire with a shape function $\Phi(r)$. Using the formula in Equation (5), we define the wire function as follows:

$$\Phi'(r) = \omega_{\rm sp} = -\sqrt{\frac{g_{rr}}{g_{00}}}\left(\frac{g_{0\phi}}{g_{\phi\phi}} + \Omega_1(r)\right), \tag{D2}$$

where $\Omega(r)$ is a function of the radial coordinate as a generalization of the Archimedean spiral shape (e.g., $\Omega_1(r) = \Omega$ is the Archimedean spiral case). We note from Equation (31) that this function has some constraints to have a physically realizable spiral step (like in the Schwarzshild metric, $\Omega_1(r) \geqslant \Omega$). Using the notation in Equation (7), the metric is

$$\begin{aligned} ds^2 &= -G_{00}\, dt^2 + G_{rr}\, dr^2 + 2G_{0r}\, dtdr \\ G_{00} &= g_{00} - (\Omega g_{\phi\phi} + 2g_{0\phi})\Omega \\ G_{rr} &= g_{rr} + \Phi'(r)^2\, g_{\phi\phi} \\ G_{0r} &= (\Omega g_{\phi\phi} + g_{0\phi})\Phi'(r). \end{aligned} \tag{D3}$$

Note that we have constraints on the values of the mass-rotation parameter $\eta = M\Omega$ and the Kerr parameter a:

$$\eta\sqrt{\frac{(1-a\eta)}{(1+a\eta)^3}} < \frac{1}{3\sqrt{3}}. \tag{D4}$$

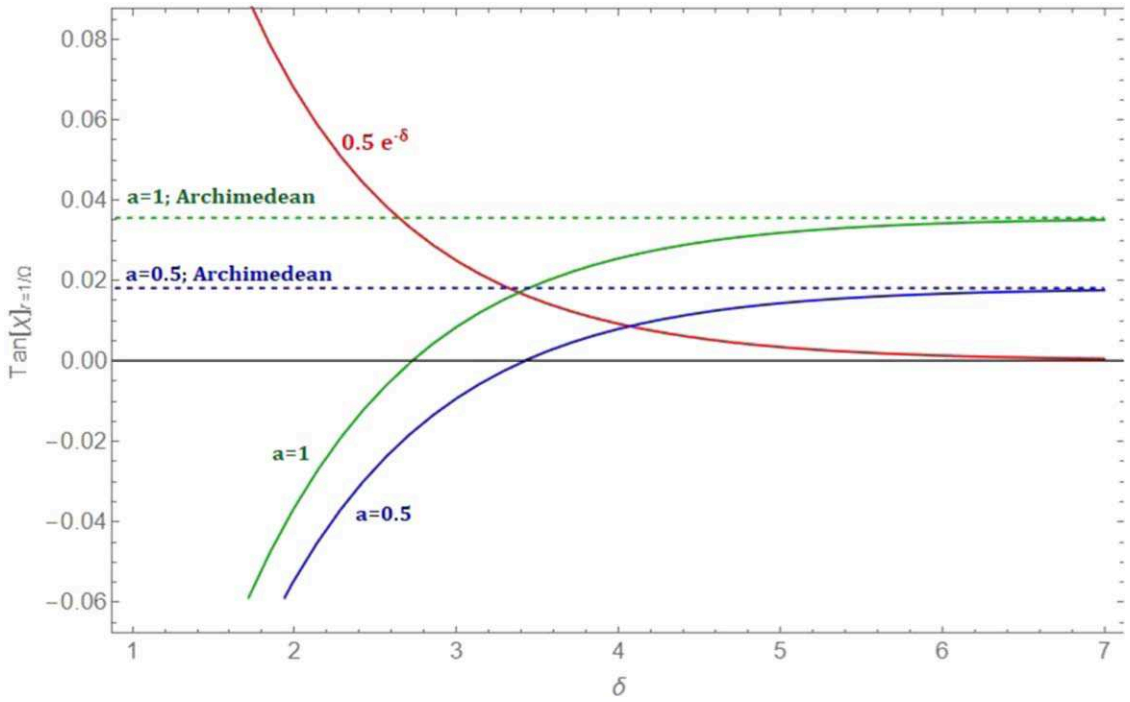

Figure 17. The ratio $\tan(\chi) = \beta_\phi/\beta_r$ (for high energy) at the outer light cylinder (in the flat case; i.e., $r = 1/\Omega$) vs. a free parameter δ to control the variation in the wire shape from the Archimedean case, for mass-rotation parameter $\eta = 0.1$. The allowed range of variation here is $\left(0, \frac{1}{2}\right]$, and is presented as an exponentially decaying function of the parameter δ, and plotted in red. We have two sets of curves corresponding to two different wire shapes: the dashed lines correspond to the Archimedean spiral case, and the solid ones correspond to a spiral that is slightly different from the Archimedean one. The colors of the curves correspond to the values of the Kerr parameter: blue curves represent $a = 0.5$ and green curves the maximally spinning black hole case ($a = 1$). For some variations, the curves meet the horizontal axis, meaning that the ratio is zero.

In the Kerr case, we have (by definition) the following coordinate basis vectors:

$$(e_0)^\mu = \begin{pmatrix} 1 \\ 0 \\ 0 \end{pmatrix} \qquad (\boldsymbol{e}_r)^\mu = \begin{pmatrix} 0 \\ 1 \\ 0 \end{pmatrix} \qquad (\boldsymbol{e}_\phi)^\mu = \begin{pmatrix} 0 \\ 0 \\ 1 \end{pmatrix}. \tag{D5}$$

Of course, these basis vectors satisfy $\boldsymbol{e}_\mu \cdot \boldsymbol{e}_\nu = g_{\mu\nu}$. The lengths are

$$|\boldsymbol{e}_\mu| = \sqrt{g_{\mu\mu}} \Rightarrow \qquad |\boldsymbol{e}_0| = \sqrt{-g_{00}} \qquad |\boldsymbol{e}_r| = \sqrt{g_{rr}} \qquad |\boldsymbol{e}_\phi| = \sqrt{g_{\phi\phi}}. \tag{D6}$$

To get the velocity components, we need to take the total (intrinsic) derivative of the normalized position vector components $\hat{V}^\mu$ (note $v^\mu := dx^\mu/dt$),

$$\frac{D}{Dt}\hat{V}^\mu = |\boldsymbol{e}_\mu|\left[\frac{d}{dt}\left(\frac{\hat{V}^\mu}{|\boldsymbol{e}_\mu|}\right) + (\Gamma^\mu_{\alpha\beta} v^\beta)\left(\frac{\hat{V}^\alpha}{|\boldsymbol{e}_\alpha|}\right)\right]. \tag{D7}$$

We obtain the velocity components as follows:

1. The radial component β_r

$$\beta_r = \frac{D}{Dt}\hat{V}^r = \frac{D}{Dt}r = v^r \times \left(1 + r\left(\frac{1}{2}\frac{d}{dr}\ln(g_{rr}) - \frac{1}{2}\frac{d}{dr}\ln(g_{rr})\right)\right) = v^r. \tag{D8}$$

   Thus, we are right about our calculations in that

$$\beta_r = \frac{Dr}{Dt} = \frac{dr}{dt}. \tag{D9}$$

2. The azimuthal component is

$$\beta_\phi = \frac{D}{Dt}\hat{V}^\phi = \frac{\sqrt{g_{rr}g_{\phi\phi}}}{2r\sin^2\theta}\left[g_{00}^2\frac{d}{dr}\left(\frac{g_{0\phi}}{g_{00}}\right) + [\beta_r\Phi'(r) + \Omega]\left(g_{00}\frac{dg_{\phi\phi}}{dr} + g_{0\phi}\frac{dg_{0\phi}}{dr}\right)\right]. \tag{D10}$$

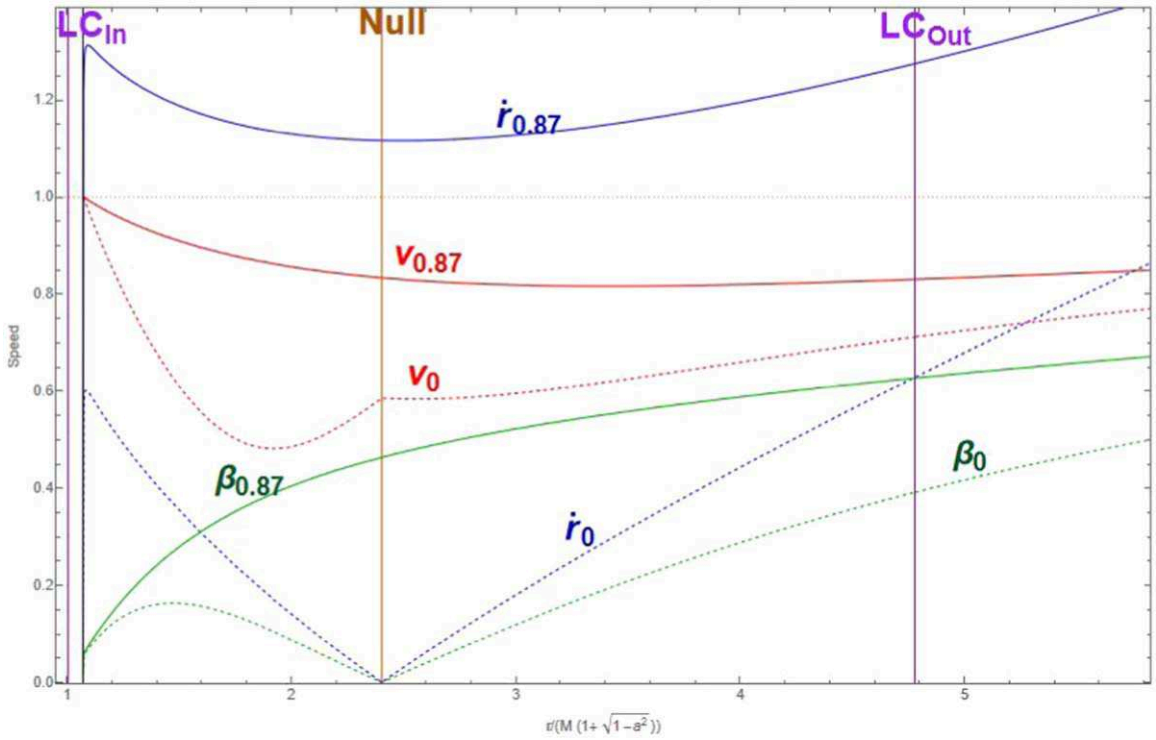

Figure 18. Various velocities for a particle moving in the Kerr black hole, in the equatorial plane for the Kerr parameter $a = 0.5$ and mass-rotation parameter $\eta = 0.1$. The coordinate r here is taken relative to the Kerr horizon $M(1 + \sqrt{1 - a^2})$. We have two sets of curves corresponding to two different initial Lorentz factors γ_{r0} in Equation (D35) at the null line: the dashed curves correspond to a zero initial speed ($\gamma_{r0} = 1$), and the solid ones correspond to an initial speed of 0.87 of the speed of light ($\gamma_{r0} \approx 2.03$). The colors of the curves correspond to the different kinds of speeds: (i) blue curves represent the proper speed, $\dot{r}$ in Equation (B4); (ii) green curves represent speed β_r, the speed measured by an observer at infinity; (iii) red curves represent the speed corresponding to the Lorentz factor in Equation (D39). The dotted (brown) horizontal line at 1 is plotted to indicate the speed of light (we see that $dr/d\tau$ exceeds the speed of light between the two light cylinders, while the other two speeds do not). The vertical lines are colored as follows: purple for both light cylinders (the inner one is so close to the Kerr horizon at 1); brown for the null line, which lies between the light cylinders; and black for the ergosphere (Equation (D27)). The ergosphere lies before the null line due to a condition on both η, a, in addition to the condition Equation (D4): $|a - \eta^{-1}| > 2\sqrt{2}$. Finally, we only plotted the speeds outside the ergosphere ($\mathcal{R} = 2M$ here) because the Lorentz factor in Equation (D39) is only defined after such radius.

The velocity vector can be written as (still working in the normalized basis)

$$\boldsymbol{v} = \beta_r \hat{\boldsymbol{e}}_r + \beta_\phi \hat{\boldsymbol{e}}_\phi. \tag{D11}$$

In the case of the Schwarzshild metric ($a = 0$),

$$\Phi'(r) = -\frac{\Omega_1(r)}{\alpha^2}. \tag{D12}$$

The velocity vector is (see how it reduces to the flat spacetime case in Equation (A3) when we have an Archimedean spiral, $\Omega_1(r) = \Omega$)

$$\boldsymbol{v} = \beta_r \boldsymbol{e}_r + r\Omega\left(\alpha - \frac{1}{\alpha}\frac{\Omega_1(r)}{\Omega}\beta_r\right)\boldsymbol{e}_\phi \qquad \underset{\alpha=1}{\overset{M=0}{\rightarrow}} \boldsymbol{v} \qquad = \beta_r \boldsymbol{e}_r + r\Omega\left(1 - \frac{\Omega_1(r)}{\Omega}\beta_r\right)\boldsymbol{e}_\phi. \tag{D13}$$

Let us calculate the ratio generally in Figure (5) in the equatorial plane

$$\tan(\chi) = \frac{\beta_\phi}{\beta_r} = \frac{\sqrt{g_{rr} g_{\phi\phi}}}{2r}\left[\frac{g_{00}^2}{\beta_r}\frac{d}{dr}\left(\frac{g_{0\phi}}{g_{00}}\right) + \left[\Phi'(r) + \frac{\Omega}{\beta_r}\right]\left(g_{00}\frac{dg_{\phi\phi}}{dr} + g_{0\phi}\frac{dg_{0\phi}}{dr}\right)\right]. \tag{D14}$$

Defining a decreasing (dimensionless) function $\delta(r)$ that is the change between the actual shape of the wire and the approximate form (the Archimedean spiral) relative to the latter:

$$\Omega_1(r) = \Omega(1 + \delta(r)) \qquad \delta(r) \ll 1\ ,\ \forall\, r \gtrapprox r_2 \qquad \lim_{r\to\infty} \delta(r) = 0. \tag{D15}$$

At very high energy ($E \to \infty$),

$$\beta_r \overset{E\to\infty}{\to} \frac{G_{00}}{G_{0r} + \sqrt{G_{00}G_{rr} + G_{0r}^2}}. \tag{D16}$$

Let us get the value of the ratio at the flat light cylinder position $r_{2;\mathrm{flat}} = 1/\Omega$ (which is close to the Kerr one, but $r_{2;\mathrm{flat}} > r_2$) for the Schwarzshild black hole and expand in small δ

$$\lim_{E\to\infty}\tan(\chi(r = 1/\Omega))_{a=0} = \frac{1}{2\eta}[(1+\delta)\sqrt{1-2\eta} - \sqrt{(1+\delta)^2 - 2\eta}] \approx \frac{-\delta}{\sqrt{1-2\eta}} \qquad \eta < \frac{1}{2}. \tag{D17}$$

In the case of the flat spacetime ($\eta \to 0$), the ratio does not depend on the rotation at all:

$$\lim_{E\to\infty}\tan(\chi(r = 1/\Omega))_{M=0} = -\frac{1}{2}\frac{\delta(\delta+2)}{\delta+1} \approx -\delta. \tag{D18}$$

In the case of a perfect Archimedean spiral, we have a zero ratio exactly in both Schwarzschild and flat spacetimes. Generally speaking, both results are close to zero for small δ. The same analysis can be done in the Kerr case, but we will not include the exact solution. Instead, we show graphically that even in the case of a maximally spinning black hole (which results in a greater value of the azimuthal speed, β_ϕ), the ratio is still close to zero, and can be exactly zero for some variation.

For plotting purposes, we consider the following possible values of the variation: $\delta(r = 1/\Omega) \in \left(0, \frac{1}{2}\right]$. Moreover, we present these possible values in the form of an exponentially decaying function $e^{-\delta}/2$, where δ here is just a free parameter, not the variation. We choose the allowed values of $\{\eta, a\}$ based on the following constraints:

$$\eta < \frac{1}{a+2\sqrt{2}} < \frac{1}{2\sqrt{2}} < \frac{1}{2} \qquad \eta\sqrt{\frac{(1-a\eta)}{(1+a\eta)^3}} < \frac{1}{3\sqrt{3}}. \tag{D19}$$

We show in Figure 17 that the small variation can cause the ratio in the Kerr case to approach zero at the flat case light cylinder position. However, this might not be the case for bigger values of η; in that case, we expect the ratio to approach zero further a bit from the light cylinder (i.e., at some finite $r > 1/\Omega$) because of the decaying nature of the ratio as a function of the radial coordinate r in general.

Moreover, far away from the light cylinder, the ratio in the Kerr case becomes

$$\lim_{E\to\infty}\tan(\chi(r \gg 1/\Omega)) \approx -\sqrt{\delta(\delta+2)} + \frac{1+\delta}{r\Omega}. \tag{D20}$$

Thus,

$$\lim_{E\to\infty}\lim_{r\to\infty}\tan(\chi) = -\sqrt{\delta(\delta+2)} \approx -\sqrt{2\delta}. \tag{D21}$$

Also, the Lorentz factor (relative to the observer at infinity) far away from the light cylinder for large energy is

$$\gamma_\beta \approx \frac{1+\delta}{\sqrt{\delta(\delta+2)}} \approx \frac{1}{\sqrt{2\delta}} \to \infty. \tag{D22}$$

Next, we calculate the Lorentz factors relative to fixed observers in spacetime and corotating observers with the wire. The Lorentz factor can be used to get the speed of the particle as a function of the distance from the black hole singularity. This speed will never exceed the speed of light, unlike the proper speed in Equation (B4), see Figure (18). We construct the Lorentz factor in curved spacetimes by imagining filling the (2+1)-D Kerr spacetime with momentarily fixed observers everywhere (only between the ergosphere and the outer light cylinder, as we will show why later). The particle anywhere between the light cylinders is at the same location as exactly one of these observers. At this point, we can obtain a dot product between the four-velocity of the fixed observer and that of the particle, and get an invariant quantity, which is the Lorentz factor of the particle as seen by the fixed observer where the particle is. The four-velocity of a fixed observer is ($\dot{t} \geqslant 0$, $\dot{r} = 0$, $\dot{\phi} = 0$)

$$U^\mu_{\mathrm{fixed}} = \begin{pmatrix} \dot{t} \\ 0 \\ 0 \end{pmatrix} \xrightarrow[\mathcal{L}=-1]{\mathcal{L}=-g_{00}\,i^2} U^\mu_{\mathrm{fixed}} = \frac{1}{\sqrt{g_{00}}}\begin{pmatrix} 1 \\ 0 \\ 0 \end{pmatrix} \Rightarrow U^{\mathrm{fixed}}_\mu = \begin{pmatrix} -\sqrt{g_{00}} & 0 & \dfrac{g_{0\phi}}{\sqrt{g_{00}}} \end{pmatrix}. \tag{D23}$$

The four-velocity of the particle is

$$U^\mu_{\mathrm{particle}} = \begin{pmatrix} \dot{t} \\ \dot{r} \\ \dot{\phi} \end{pmatrix} = \begin{pmatrix} \dot{t} \\ \dot{r} \\ \Phi'(r)\dot{r} + \Omega\dot{t} \end{pmatrix}. \tag{D24}$$

The relative Lorentz factor observed by such fixed observes for the particle is

$$\gamma = -U^{\rm fixed}_{\mu} U^{\mu}_{\rm particle} = \left(\sqrt{g_{00}} - \frac{\Omega g_{0\phi}}{\sqrt{g_{00}}}\right)\dot{t} - \frac{\Phi'(r) g_{0\phi}}{\sqrt{g_{00}}}\dot{r}. \tag{D25}$$

From both Equations (B2) and (B4), the Lorentz factor becomes

$$\gamma = \left(\sqrt{g_{00}} - \frac{\Omega g_{0\phi}}{\sqrt{g_{00}}}\right)\frac{E}{G_{00}} \pm \left(\left(\sqrt{g_{00}} - \frac{\Omega g_{0\phi}}{\sqrt{g_{00}}}\right)\frac{G_{0r}}{G_{00}} - \frac{\Phi'(r) g_{0\phi}}{\sqrt{g_{00}}}\right)\sqrt{\frac{E^2 - G_{00}}{G_{0r}^2 + G_{00}\, G_{rr}}}. \tag{D26}$$

The negative (positive) sign means that the particle is moving toward (away from) the black hole. This Lorentz factor is only defined whenever g_{00} is positive; i.e., outside the ergosphere

$$\mathcal{R} = M(1 + \sqrt{1 - a^2 \cos^2\theta}). \tag{D27}$$

See Figure 18 for a plot of the speed of the particle observed by the fixed observers, which can be obtained from the relation

$$\gamma = \frac{1}{\sqrt{1 - v^2}}. \tag{D28}$$

We have a range of allowed values for the constant of motion E. Let r_1 and r_2 be the locations of the light cylinders. From Equation (B4), we get

$$0 < G_{00} \leqslant E^2, \qquad r \in (r_1, r_2) \tag{D29}$$

$$\Omega^2 r^3 - (1 - a^2\eta^2 - E^2) r + 2M(1 - a\eta)^2 \geqslant 0. \tag{D30}$$

This is a cubic equation on the form $\Omega^2 r^3 - br + d = 0$ that has to always be non-negative, for all the positive values of r. Therefore, we need to guarantee that the minimum (i.e., extreme) value of the cubic function is also non-negative. We obtain

$$\Omega^2 r^3 - br + d \geqslant 0, \qquad b > 0, d \geqslant \frac{1}{3\sqrt{3}}\frac{2b^{\frac{3}{2}}}{\Omega} \tag{D31}$$

$$\begin{cases} \sqrt{1 - a^2\eta^2 - 3\eta^{\frac{2}{3}}(1 - a\eta)^{\frac{4}{3}}} \leqslant E & r \in (r_1, r_2) \\ 0 \leqslant E < \infty & r > r_2 \end{cases}. \tag{D32}$$

The time constant E that appears in Equation (D26) can be related to the initial conditions as observed by a set of fixed observers along the rotating wire. We imagine a set of fixed observers along the rotating wire, only defined between the two light cylinders, and they observe the particle radial speed only. We obtain the relative Lorentz factor as seen by the observers along the wire by applying the same procedure we used to get Equation (D26), but now on the (1+1)-D sub-manifold. The four-velocity of a fixed observer is ($\dot{t} \geqslant 0$, $\dot{r} = 0$)

$$U^{\mu}_{\rm fixed} = \begin{pmatrix} \dot{t} \\ 0 \end{pmatrix} \xrightarrow[\mathcal{L}=-1]{\mathcal{L}=-g_{00}\,\dot{t}^2} U^{\mu}_{\rm fixed} = \frac{1}{\sqrt{G_{00}}}\begin{pmatrix} 1 \\ 0 \end{pmatrix} \Rightarrow U^{\rm fixed}_{\mu} = \begin{pmatrix} -\sqrt{G_{00}} & \dfrac{G_{0r}}{\sqrt{G_{00}}} \end{pmatrix}. \tag{D33}$$

The four-velocity of the particle is

$$U^{\mu}_{\rm particle} = \begin{pmatrix} \dot{t} \\ \dot{r} \end{pmatrix} \quad \xrightarrow{(B2)} \quad U^{\mu}_{\rm particle} = \begin{pmatrix} \dfrac{G_{0r}\,\dot{r} + E}{G_{00}} \\ \dot{r} \end{pmatrix}. \tag{D34}$$

The radial Lorentz factor of the radially moving particle relative to the fixed observers (on the wire) is the invariant quantity

$$\gamma_r = -U^{\rm fixed}_{\mu} U^{\mu}_{\rm radial} = \frac{E}{\sqrt{G_{00}}} = \frac{1}{\sqrt{1 - v_r^2}}. \tag{D35}$$

As expected, the radial Lorentz factor coincides with the total one in Equation (D26) in the case of a nonrotating wire:

$$\gamma = \gamma_r = \frac{E}{\sqrt{G_{00}}} = \frac{E}{\sqrt{g_{00}}} \ (\Omega = 0). \tag{D36}$$

Since the Lorentz factor is always positive, the constant E is always positive too. We can get E easily from the initial conditions as seen by a fixed observer along the wire. If such an observer is at r_0 observes the particle moving along the wire a radial Lorentz factor γ_{r0}, we obtain[1]

$$E = \gamma_r \sqrt{G_{00}} = \gamma_{r0} \sqrt{G_{00}(r_0)}. \tag{D37}$$

The Lorentz factor in Equation (D26) becomes

$$\begin{aligned}\gamma &= \frac{E}{G_{00}}\left[\left(\sqrt{g_{00}} - \frac{\Omega g_{0\phi}}{\sqrt{g_{00}}}\right) \pm \frac{v_r}{\sqrt{G_{0r}^2 + G_{00}\, G_{rr}}}\right.\\ &\left.\times\left(\left(\sqrt{g_{00}} - \frac{\Omega g_{0\phi}}{\sqrt{g_{00}}}\right)G_{0r} - \frac{\Phi'(r) g_{0\phi}}{\sqrt{g_{00}}} G_{00}\right)\right]\\ &= \frac{\gamma_r}{\sqrt{G_{00}}}\left[\left(\sqrt{g_{00}} - \frac{\Omega g_{0\phi}}{\sqrt{g_{00}}}\right) \pm \frac{v_r}{\sqrt{G_{0r}^2 + G_{00}\, G_{rr}}}\right.\\ &\left.\times\left(\left(\sqrt{g_{00}} - \frac{\Omega g_{0\phi}}{\sqrt{g_{00}}}\right)G_{0r} - \frac{\Phi'(r) g_{0\phi}}{\sqrt{g_{00}}} G_{00}\right)\right]\end{aligned} \tag{D38}$$

$$\begin{aligned}\gamma = \gamma_{r0}\, &\frac{\sqrt{G_{00}(r_0)}}{G_{00}}\left(\sqrt{g_{00}} - \frac{\Omega g_{0\phi}}{\sqrt{g_{00}}}\right)\pm\\ &\left(\left(\sqrt{g_{00}} - \frac{\Omega g_{0\phi}}{\sqrt{g_{00}}}\right)\frac{G_{0r}}{G_{00}} - \frac{\Phi'(r) g_{0\phi}}{\sqrt{g_{00}}}\right)\sqrt{\frac{\gamma_{r0}^2 G_{00}(r_0) - G_{00}}{G_{0r}^2 + G_{00}\, G_{rr}}}.\end{aligned} \tag{D39}$$

We imagine ejecting the particles on the outer light cylinder ($r = r_2$) with an initial Lorentz factor γ_0 as the initial conditions. Then, we solve for the energy E:

$$\begin{aligned}\gamma_0 = \lim_{r\to r_2}\gamma &= \frac{1}{2E}\left(\sqrt{g_{00}} - \frac{\Omega g_{0\phi}}{\sqrt{g_{00}}}\right)_{r_2}\\ &\times\left(1 + G_{rr}\left(\frac{E}{G_{0r}}\right)^2\right)_{r_2} - \left(\frac{\Phi'(r) g_{0\phi}}{\sqrt{g_{00}}}\frac{E}{|G_{0r}|}\right)_{r_2}\end{aligned} \tag{D40}$$

$$E = \left\{\frac{\gamma_0 \pm \sqrt{\gamma_0^2 - \left(\sqrt{g_{00}} - \frac{\Omega g_{0\phi}}{\sqrt{g_{00}}}\right)\left[\left(\sqrt{g_{00}} - \frac{\Omega g_{0\phi}}{\sqrt{g_{00}}}\right)\frac{G_{rr}}{G_{0r}^2} - \frac{2}{|G_{0r}|}\frac{\Phi'(r) g_{0\phi}}{\sqrt{g_{00}}}\right]}}{\left(\sqrt{g_{00}} - \frac{\Omega g_{0\phi}}{\sqrt{g_{00}}}\right)\frac{G_{rr}}{G_{0r}^2} - \frac{2}{|G_{0r}|}\frac{\Phi'(r) g_{0\phi}}{\sqrt{g_{00}}}}\right\}_{r_2}. \tag{D41}$$

Therefore, we see that there has to be a minimum initial Lorentz factor for the constant E to have real values. Moreover, we only need the larger energy of the two solutions to guarantee that we have a solution between the light cylinders as well, by being consistent with the constraints (Equation (D32)). Usually, we have a large Lorentz factor when the particle reaches the outer light cylinder; thus, giving the particle an initial push at the outer light cylinder with a relatively large γ_0 will result in a large amount of the energy:

$$E \approx \gamma_0\left(\frac{2G_{0r}^2}{\left(\sqrt{g_{00}} - \frac{\Omega g_{0\phi}}{\sqrt{g_{00}}}\right)G_{rr} - 2|G_{0r}|\frac{\Phi'(r) g_{0\phi}}{\sqrt{g_{00}}}}\right)_{r_2} \sim \gamma_0. \tag{D42}$$

For large values of the Lorentz factor of the particle at the outer light cylinder, the energy of the particle behaves the same way as the Lorentz factor of the particle at the outer light cylinder.

[1] For clarity, the difference between γ_{r0} and γ is that the former is obtained by the observers along (and rotating with) the wire (i.e., in the (1+1)-D sub-manifold); the latter, γ, is obtained by the observers fixed on the Kerr spacetime (i.e., in the (2+1)-D manifold), which contains both the radial and the rotational parts of the speed of the particle.

ORCID iDs

Maxim Lyutikov https://orcid.org/0000-0001-6436-8304
Ahmad Ibrahim https://orcid.org/0009-0008-7401-5682

References

Bardeen, J. M., Press, W. H., & Teukolsky, S. A. 1972, ApJ, 178, 347
Barkov, M. V., & Komissarov, S. S. 2008, MNRAS, 385, L28
Beskin, V. S. 2009, MHD Flows in Compact Astrophysical Objects: Accretion, Winds and Jets (Berlin: Springer)
Beskin, V. S., Istomin, Y. N., & Parev, V. I. 1992, SvA, 36, 642
Beskin, V. S., & Kuznetsova, I. V. 2000, NCimB, 115, 795
Bicknell, G. V., & Begelman, M. C. 1996, ApJ, 467, 597
Birdsall, C. K., & Langdon, A. B. 1991, Plasma Physics via Computer Simulation (Bristol: Adam Hilger)
Blandford, R., Meier, D., & Readhead, A. 2019, ARA&A, 57, 467
Blandford, R. D., & Königl, A. 1979, ApJ, 232, 34
Blandford, R. D., & Payne, D. G. 1982, MNRAS, 199, 883
Blandford, R. D., & Znajek, R. L. 1977, MNRAS, 179, 433
Boris, J. P., & Roberts, K. V. 1969, JCoPh, 4, 552
Camenzind, M. 1986, A&A, 162, 32
Chen, A. Y., & Beloborodov, A. M. 2014, ApJL, 795, L22
Clausen-Brown, E., Lyutikov, M., & Kharb, P. 2011, MNRAS, 415, 2081
Comisso, L., & Asenjo, F. A. 2021, PhRvD, 103, 023014
Contopoulos, I., Pétri, J., & Stefanou, P. 2020, MNRAS, 491, 5579
Crinquand, B., Cerutti, B., Philippov, A., Parfrey, K., & Dubus, G. 2020, PhRvL, 124, 145101
Goldreich, P., & Julian, W. H. 1970, ApJ, 160, 971
Grad, H. 1967, PhFl, 10, 137
Gralla, S. E., & Jacobson, T. 2014, MNRAS, 445, 2500
Gruzinov, A. 2007, arXiv:0710.1875
Hakobyan, H., Philippov, A., Spitkovsky, A., et al. 2023, ApJ, 943, 105
Hirotani, K., & Okamoto, I. 1998, ApJ, 497, 563
Kim, J. Y., Krichbaum, T. P., Lu, R. S., et al. 2018, A&A, 616, A188
Komissarov, S. S. 2004, MNRAS, 350, 427
Komissarov, S. S., Vlahakis, N., Königl, A., & Barkov, M. V. 2009, MNRAS, 394, 1182
Krolik, J. H. 1999, Active Galactic Nuclei: from the Central Black Hole to the Galactic Environment (Princeton, NJ: Princeton Univ. Press)
Landau, L. D., & Lifshitz, E. M. 1975, The Classical Theory of Fields (Oxford: Pergamon)
Levinson, A. 2000, PhRvL, 85, 912
Levinson, A., & Rieger, F. 2011, ApJ, 730, 123
Lu, R.-S., Asada, K., Krichbaum, T. P., et al. 2023, Natur, 616, 686
Lyutikov, M. 2003, MNRAS, 346, 540
Lyutikov, M. 2009, MNRAS, 396, 1545
Lyutikov, M. 2022, ApJL, 933, L6
Lyutikov, M., Pariev, V. I., & Gabuzda, D. C. 2005, MNRAS, 360, 869
McKinney, J. C. 2006, MNRAS, 368, 1561
Michel, F. C. 1969, ApJ, 158, 727
Michel, F. C. 1973, ApJL, 180, L133
Misner, C. W., Thorne, K. S., & Wheeler, J. A. 1973, Gravitation (San Francisco, CA: W.H. Freeman)
Nakamura, M., & Asada, K. 2013, ApJ, 775, 118
Nokhrina, E. E., & Beskin, V. S. 2017, MNRAS, 469, 3840
Philippov, A. A., Spitkovsky, A., & Cerutti, B. 2015, ApJL, 801, L19
Prokofev, V. V., Arzamasskiy, L. I., & Beskin, V. S. 2018, MNRAS, 474, 1526
Ptitsyna, K., & Neronov, A. 2016, A&A, 593, A8
Ripperda, B., Liska, M., Chatterjee, K., et al. 2022, ApJL, 924, L32
Scharlemann, E. T., & Wagoner, R. V. 1973, ApJ, 182, 951
Shafranov, V. D. 1966, RvPP, 2, 103
Spitkovsky, A. 2006, ApJL, 648, L51
Tomimatsu, A. 1994, PASJ, 46, 123